UNIVERSITY OF HELSINKI

https://helda.helsinki.fi

Drought in a warmer, CO2-rich climate restricts grassland water use and soil water mixing

Radolinski, Jesse; Vremec, Matevz; Wachter, Herbert; Birk, Steffen; Brüggemann, Nicolas ...

2025-01-17
American association for the advancement of science
http://hdl.handle.net/10138/627414
Radolinski, J, Vremec, M, Wachter, H, Birk, S, Brüggemann, N, Herndl, M, Kahmen, A, Nelson, D B, Kübert, A, Schaumberger, A, Stumpp, C, Tissink, M, Werner, C & Bahn, M 2025, 'Drought in a warmer, CO 2 -rich climate restricts grassland water use and soil water mixing', Science, vol. 387, no. 6731, pp. 290-296. https://doi.org/10.1126/science.ado0734

Downloaded from Helda, University of Helsinki institutional repository. https://helda.helsinki.fi
This is an electronic reprint of the original article.
This reprint may differ from the original in pagination and typographic detail.
Please cite the original version.

Drought in a warmer, CO_2-rich climate restricts grassland water use and soil water mixing

Jesse Radolinski[12]*, Matevz Vremec[3], Herbert Wachter[1], Steffen Birk[3], Nicolas Brüggemann[4], Markus Herndl[5], Ansgar Kahmen[6], Daniel B. Nelson[6], Angelika Kübert[7], Andreas Schaumberger[5], Christine Stumpp[8], Maud Tissink[1], Christiane Werner[9], and Michael Bahn[1]

Affiliations:
[1]Department of Ecology, University of Innsbruck; Sternwartestraße 15, A-6020 Innsbruck, Austria
[2]Department of Environmental Science and Technology, University of Maryland; 1443 Animal Sciences Building, 8127 Regents Dr, College Park, MD 20742, USA
[3]Department of Earth Sciences, NAWI Graz Geocenter; University of Graz, Graz 8010, Austria
[4]Forschungszentrum Jülich GmbH, IBG-3; Wilhelm-Johnen-Straße, 52428 Jülich, Germany
[5]Agricultural Research and Education Center (AREC) Raumberg-Gumpenstein; Raumberg 38, A-8952 Irdning-Donnersbachtal, Austria
[6]Department of Environmental Sciences – Botany, University of Basel; Schönbeinstrasse 6, 4056 Basel, Switzerland
[7]Faculty of Science, Institute for Atmospheric and Earth System Research/Physics, University of Helsinki; PO Box 68, Gustaf Hällströmin katu 2b, Helsinki, 00014 Finland
[8]University of Natural Resources and Life Sciences, Vienna, Department of Water, Atmosphere and Environment, Institute of Soil Physics and Rural Water Management; Muthgasse 18, 1190 Vienna, Austria
[9]Ecosystem Physiology, University of Freiburg; 79098 Freiburg, Germany
*Corresponding author. Email: jradolin@umd.edu

Abstract: Soil water sustains terrestrial life, yet its fate is uncertain under a changing climate. We conducted a deuterium labeling experiment to determine if elevated atmospheric CO_2, warming, and drought impact soil water storage and transport in a temperate grassland. Elevated CO_2 created a wetter rootzone compared to ambient conditions, whereas warming decreased soil moisture. Soil water remained well-mixed in all global change treatments except for summer drought combined with warming and elevated CO_2. These combined treatments caused the grassland to conserve water and restricted soil water flow to large, rapidly draining pores without mixing with small, slowly draining pores. Our results suggest that drought in a warmer, more CO_2-rich climate can severely alter grassland ecohydrology by constraining post-drought soil water flow and grassland water use.

One-Sentence Summary: Drought in a warmer, more CO_2-rich climate restricts grassland water use and soil water mixing.

Main Text: Rootzone soil water represents just 0.001% of Earth's total and 0.05% of its freshwater resources (*1*), but exerts a disproportionate control on terrestrial biogeochemical cycling (*2, 3*), surface energy balance (*4*), and plant productivity (*5, 6*). Accurate soil water records thus underpin our ability to assess the ecohydrological impacts of climate change (*7, 8*). Through soils, precipitation is either returned – mainly via evaporation and transpiration- to the atmosphere or transported to surface or groundwater bodies based on an interplay of pressure gradients and intrinsic soil properties (e.g., soil texture and structure). Climate change could alter these storage and flow properties (*9*). Atmospheric warming may amplify water vapor pressure gradients at the soil or leaf surface, increasing evapotranspiration (*10*) and soil water loss (*11*). Alternatively, elevated atmospheric CO_2 can decrease rootzone water loss (*12*) by reducing the aperture of plant stomata and lowering transpiration rates (*13, 14*). Warming with elevated CO_2, however, could produce mixed hydrological responses, from prolonged dry periods (*15*) to drought alleviation despite higher temperatures (*16, 17*). Prolonged, extreme drying may lower soil water retention (*18*).

As terrestrial ecosystems are increasingly exposed to severe drought (*19, 20*) in a warmer (*21*), more CO_2-rich atmosphere (*16*), the need to quantify the impacts of these factors on soil hydrology increases. Climate manipulation experiments have advanced our understanding of global change effects on ecosystem functioning; however, comprehensive analyses of drought impacts on ecohydrological processes under future conditions such as elevated CO_2 and warming are lacking (*14, 18, 22-24*). Tracing the source and "age" (i.e., time since precipitation) of soil water under various climate manipulations may reveal alterations to plant water use or soil physical properties (*25*).

Conventional assumptions hold that transpiration, groundwater, and stream water are connected through a well-mixed reservoir of rootzone soil water (*26, 27*), whereby new precipitation mixes with or displaces "older" resident water en route to streams. Contrary to these assumptions, stable isotope studies (*28-30*) propose that an ecohydrological separation (*31*) between streams and plants often arises as flow paths conduct water past rootzone storage without mixing. New evidence, however, suggests that even under extreme precipitation events (*32*) this separation is not in line with the current understanding of soil physics (*32, 33*). A projected future climate with more hydrological extremes (*20*) increases the need to understand these processes, yet underlying mechanisms remain poorly defined.

Grasslands cover 30-40% of Earth's terrestrial surface and, as shallow-rooted communities, they are particularly reliant on shallow soil water (*34*) and ideal for studying ecohydrological rootzone dynamics. We conducted a deuterium labelling experiment in a temperate grassland (Styria, Austria; **Fig. S1**; (*35, 36*)) to study how individual and combined effects of 1) atmospheric CO_2 enrichment (+300 ppm), 2) warming (+3°C) (1 and 2 follow Representative Concentration Pathway 6.0 (*37*)), and 3) recurring drought (**Table S1**) alter the transport and ecohydrological partitioning of precipitation through the rootzone. Following an experimental drought in summer 2021, we supplied ^{2}H-labeled rainfall to replicated treatments (n = 3-6 per treatment) under ambient climate, individual and combined ("future") warming and elevated CO_2, as well as recurring ambient and future drought. We then 1) used six months of continuous soil hydrological monitoring and high resolution (4h) rootzone water isotopic signatures to model (HYDRUS 1D (*38*), H1D) to quantify soil water transport processes, and 2) performed additional isotopic monitoring of evaporative fluxes (transpiration and evapotranspiration) to partition the sources of plant water use.

Climate manipulation imposes differences in soil water quantity and source water

Soil water content (θ; depth-weighted from 0-36 cm) in the rootzone remained lower for treatments with drought or warming compared to ambient (control) conditions and higher for elevated CO_2 without warming (**Fig. 1A**). As the grassland periodically dried, all treatments displayed older source water in storage (**Fig. 1B**) and evaporative fluxes (**Fig. 1C**), which – before the label was applied— resembled isotopically-lighter, earlier-season precipitation signatures. However, these effects were amplified under peak (late July) drought and a natural dry period in mid-September. By rewetting the soil profile with 40 mm of ^{2}H-labeled water (August 2nd; 75 mm h^{-1}; δ^2H = 3300 ‰), we traced the fate of precipitation across the experimental treatments.

Drought alters subsequent water transport in grasslands under elevated CO_2 and warming

We expected that soils experiencing extreme drying, followed by intense precipitation, would display initial isotope signatures that reflect the event water—since little pre-event storage exists to dilute incoming precipitation (*39*). Accordingly, the rewetting signature would dissipate as subsequent precipitation mixes with (*40*), displaces (*32*), or evapotranspiration removes (*41*) this storage. The future drought treatment, however, produced an unexpected pattern of water transport (**Fig. 1B**). ^{2}H-labeled water in the future drought treatment entered the finer pores of the soil matrix and remained in the rootzone up to 125 d without being displaced by new precipitation and drainage events through early autumn (**Fig. S2**). The time elapsed from the rewetting event to peak label signatures at 36 cm was 25-fold greater for the future versus ambient drought (**Fig. S2**).

To interpret this behavior, we examined how the soil-plant system responded to drought. Although the ambient drought had greater evapotranspiration (**Figs. S3** and **S4**) and drawdown of rootzone water (**Fig. 1A**), elevated pre-drought evapotranspiration for the future drought treatment produced an overall greater water deficit by the end of the drought (0-60 cm; **Fig. 2A**). The future drought treatment also regularly underwent more extreme seasonal drying (**Table S1**). Further, we detected the lowest transpiration rates relative to total evapotranspiration (T/ET) during peak drought for the future drought treatment –60% lower than the corresponding non-drought conditions (p = 0.06; **Fig. 2B**). Recurring future drought conditions not only altered soil

water movement but also affected plant water use during and following the drought (**Figs. 2B** and **2C**).

Shortly after rewetting with δ^2H_2O, the future drought treatment produced the highest δ^2H values in evapotranspiration (**Fig. 1C**) as labeled water entered the entire soil pore space (**Fig. S5**). The tracer signal in all global change scenarios subsided towards pre-label values after 30 days in transpiration and evapotranspiration (**Fig. 1D**), as would be expected by steady-state, advection-dispersion-based transport from soil to plants (**Fig. 2C**). Evaporative fluxes were, thus, more dependent on new precipitation than water introduced during the label event. Indeed, our process-based (H1D) depiction of water movement through the grassland was greatly improved for the future drought scenario after limiting tracer removal through transpiration (**Tables S1 to S5**, **Fig. S6**). Low evapotranspiration (**Fig. S4**), T/ET (**Fig. 2B**), and high residual tracer mass in deep rootzone drainage (**Fig. 3A**) further suggest that the grassland exposed future drought decreased water loss through evapotranspiration and reduced transpiration of labeled water. As a result, 91% of the applied tracer in the future drought treatment left the lower rootzone (36 cm depth) as drainage after 200 days of monitoring, compared to 44% in the elevated CO_2 and warming, and 40% in ambient drought treatments (H1D results; **Fig. 3A**). Interestingly, this labeled water was redistributed upward in the soil profile (**Fig. S5**) and re-supplied transpiration (**Fig. 1C**) in all treatments during a natural dry period 44 days after rewetting (**Fig. 2C**). The shift in water use, however, was most extreme for the future drought ($p < 0.05$, **Figs. 1C** and **2C**), even after accounting for varying evaporative fluxes (**Fig. S7**). Contrary to steady-state transport assumptions, these data highlight the ecohydrological plasticity of grassland water use in a warmer, more drought-prone climate.

Further, soil water transport processes differed between treatments. The best-fit H1D results indicate that the proportion of the tracer water leaving the lower rootzone as drainage was far greater (and occurred for far longer) in the future drought than other treatments (**Fig. 3A**). The median water transit time (water exit minus entry times) of the future drought treatment was nearly three times that of its non-drought counterpart (elevated CO_2 and warming alone) (**Fig. 3A**). Additionally, greater modelled differences between water transport normalized to filled versus partially-filled pore volumes (**Fig. 3B**), suggest that the bulk of tracer movement in the future drought treatments was likely restricted to a smaller fraction of soil pore space.

Future drought creates hydrological disconnection in pore space

To further explore possible hydrological anomalies in the rootzone, we compared our soil water isotopic observations to those of a "well-mixed" system, where incoming precipitation completely mixed with pre-precipitation-event soil water across the post-label period (**Fig. 4**). Weighted soil water δ^2H for non-drought treatments nearly match homogenous mixing projections. By contrast, the measured ambient drought treatment values deviated from the mixing projection through the natural dry period (i.e., September 1^{st}-15^{th}), but exhibited strong mixing dynamics later in the monitoring period. The future drought treatment, however, showed a lack of mixing for the entire post-drought period (**Fig. 5**).

Our high-resolution soil water isotope measurements (**Fig. 1B**) are "bulk" soil water signatures which integrate all pores (*42*); however, this pore space can be further isolated using water tension (negative pressure). We compared bulk soil water signatures to replicated suction lysimeter samples (600 cm of tension; pore diameter >5 µm) which incorporate mobile soil water (*28*) from larger pores (**Fig. S8**). Most climate manipulations showed pronounced differences between mobile and bulk soil water directly after the labeled precipitation (up to 2500 ‰ δ^2H; **Fig. S9**) which dissipated after 10 days. The combination of elevated CO_2, warming, and drought, however, produced the greatest separations ($p < 0.0001$; 18 cm) (**Fig. S9**), such that mobile water resembled recent rainfall signatures more than bulk soil water. Considering our extensive tracer records (high-resolution: **Fig. 1B**; n = 3-6 replicate plots per treatment: **Figs. 1C, S8**, **S9**, **S10**, and **S11**), and background variation therein (e.g., **Fig. 3**), the future drought treatment clearly restricted hydrological exchange across soil pore space. Further, the future drought system had a greater proportion of large pores that rapidly drained under gravitational force (i.e., macropores) (**Fig. S12**), which may have sustained this disconnection (**Fig. 5, F, I,** and **L**). Thus, multiple lines of evidence indicate that future drought conditions subsequently altered water flow paths in the rootzone, resulting in rapid water flow in larger pores and little mixing with finer pores in the soil matrix—severely limiting hydrological connectivity.

The hydrological disconnections in this study challenge current understanding of flow heterogeneity and mixing in soils. Soil water was well-mixed in all but the drought scenario amplified (**Fig. 2A**) by future climate conditions (**Fig. 4**), suggesting that ecohydrological separation (via pore water separation) is unlikely in the absence of extreme hydrological conditions (*32*). Lower rootzone (36 cm) isotopic signatures (post-label; **Fig. 1B**) in the future drought treatment remained relatively constant for >100 d despite frequent rainfall, and weighted soil water signatures differed from that of a well-mixed system by a factor of up to 800 (**Fig. 4**). When scaled for respective ranges of precipitation isotope signatures, mobile versus bulk soil water separation in our study was three times greater than some of the highest recorded thus far (e.g., (*28*)).

Implications of global change: an ecohydrological perspective

These altered soil hydrological processes induced by future drought conditions have strong ecohydrological repercussions for the fate of rootzone water. When available under wetter conditions, the future drought treatment returned younger, mobile (**Fig. S9**), and likely more well-mixed (**Figs. 1** and **2**) water to the atmosphere but relied on relatively older soil-matrix-derived water during the natural dry period in (**Fig. 2**). A recent continental-scale synthesis (*43*) of evapotranspiration water ages suggests that plant communities extracting younger water may recover transpiration rates faster following drought but maintain lower vegetation water storage. Contrastingly, older-transpiring systems recover slowly from disturbance but maintain more stable plant water content. Thus, the variable sourcing of water (**Figs. 5F, 5I,** and **5L**) in the future drought system may maximize ecosystem resilience at the expense of plant growth and throughput (*43*) (reduced evapotranspiration, **Fig. S3** and lower T/ET, **Fig. 2**).

Intense drying can trigger high hydraulic gradients where previous event-water is stored in small soil pores under orders of magnitude higher tension than the largest pores (*44, 45*). Following

precipitation, unstable wetting fronts and macroporous subsurface architectures create heterogeneous soil water flow, where whole pore regions are often bypassed (*32, 46, 47*). This can create contrasts in water age across the pore space, where small pores – because they fill first and drain last – retain "older" storage relative to larger pores, which rapidly conduct younger mobile water from recent precipitation (*48*) (**Fig. 5**). Thus, plants may regularly access water which requires the least energy to extract (*49*): young, well-mixed, low-tension water under wet conditions and older, high-tension water from finer pores during dry conditions. Analogously, the soil water drainage of such systems will express the same "younger-wetter" and "older-drier" dynamics (*50*). Contrary to current ecohydrological separation assumptions (*28, 30, 51*) that plants generally prefer high-tension water in the soil matrix, plants with disconnected (unmixed) soil pore waters accessed this high-tension water only during the onset of rapid drying (**Fig. 5I**). Drought-exposed treatments displayed the greatest hydrological separations in pore space; however, the extreme disconnection seen in the future scenario suggests that altered soil physical properties exacerbated this effect. Intense wetting and drying cycles (*52*) in this recurrent future drought treatment created a macroporous soil (**Fig. S10**), whose structural orientation reduced water exchange between the finest and coarsest pores (**Fig. 5l**). Slightly elevated levels of soil organic carbon in the deeper rootzone (**Fig. S10**— potentially driven by elevated CO_2 (*53*) and carbon transfer (*54*) to drought-resistant symbionts (e.g., mycorrhizae) (*55, 56*)— may have then stabilized this altered pore network (*57*).

Warming produced rapid drying of the rootzone (**Figs. 1** and **S3**), whereas elevated CO_2 triggered reductions in transpiration (**Figs. S3** and **S4**), especially during periods of water-limitation (*58, 59*), consistent with our earlier observations (*58, 60*). Combining these two factors with drought reduced evapotranspiration further and caused an accumulation of older water storage in the rootzone (*50*), which intensified the old-young water contrast in pore space. Further testing for direct, plant-driven effects on evapotranspiration, revealed that the grassland previously exposed to future drought conditions did not alter leaf area index (**Fig. S13**), but decreased water use more strongly than in other treatments on days when atmospheric water demand (i.e., vapor pressure deficit, VPD) was high (**Fig. S14A**). This was due to an increased sensitivity of canopy conductance to VPD (**Fig. S14B**), most likely in response to the reduced root water access in this treatment, as previously observed for stomatal sensitivity to VPD (*49, 61*). Widespread transitions to water limitation (*62, 63*) and more frequent droughts (*20, 64*) under a warmer, more CO_2-rich climate will likely increase the relevance of these phenomena.

We provide a window into potential future mechanisms of soil-plant water interactions and thoroughly document mixing restrictions in soils—a topic intensely debated in current water research (*28, 32, 33, 65, 66*). These results refine our understanding of mixing in the soil-plant-atmosphere continuum and have significant repercussions for projecting future availability and flow of near-surface water and its consequences for ecosystem functioning

Acknowledgements

We thank the ClimGrass and ClimGrassHydro team for invaluable contributions to this study: including Veronika Forstner, Camille Halais, Johannes Cunow, Medardus Schweiger, Jeremy Mempiot, Marie Plakolb, Alexandra Geiger, Martina Schink, Franziska Schrempf, and Matthias Kandolf. Thanks to Gurpal S. Toor and Ryan D. Stewart for initial feedback on manuscript figures. **Funding**: This work was funded by the Austrian Academy of Sciences (ÖAW-ESS-project ClimGrassHydro) led by M.B., and supplemented by the Tyrolean Science Foundation led by JR (F. 33781/9-2021). **Author contributions:** M.B. designed the background experiment and initiated and gained funding for the study, with input from S.B. The study was co-designed by M.B. and J.R., with critical contributions from C.W., N.B., C.S., Ansgar K., Angelika K., S.B., M.H., A.S., and M.V. Experimentation was led by J.R., with help from H.W., A.S., M.T., and M.H. Data analysis was led by J.R. with help from D.N., Ansgar K., MB, M.V., M.H., and further input from all other authors. M.V., led the H1D inverse modeling procedure in close cooperation with S.B., C.S., and J.R. H.W. led the design and implementation of the membrane tube-isotope measuring system with input from J.R., M.B. N.B., Angelika K., and C.W. J.R. led the writing, with input from M.B. and feedback from all authors. **Competing interests**: Authors declare no competing interests. **Data and materials availability**: All data and computer code needed to reproduce results (*67*) are publicly available at: http://datadryad.org/stash/share/si22ZWekx4W_0intZ5bny1A1bcSGQElQF4IYQbhJ7Ig.

Supplementary Materials

Materials and Methods
Supplementary Text
Figs. S1 to S17
Tables S1 and S5
References (*66*–*123*)

Fig. 1. Water isotope (δ^2H) values in soil, evapotranspiration (ET), and transpiration (T) water, with precipitation (p) and soil water content (θ). **A** shows the weekly δ^2H values (top panel) and daily accumulation of precipitation (inverse y axis), underlain by the combined, and daily, depth-weighted θ from 0-36 cm using 3, 9, 18, and 36 cm measurements (θ; n = 2 per treatment). The distribution of δ^2H measured in water vapor (**B**) below- (n = 1 per treatment and depth) and (**C**) above-ground δ^2H (n values per treatment and sampling plotted in the bottom panel) throughout the monitoring period of 2021-2022. Note that the displayed precipitation (**A**) applies to all treatments, except for the "Drought" treatments during the experimental drought period (yellow panel in **A**) where rainfall was suppressed for all but one event on 2021-06-21. Black borders in **C** denote evapotranspiration (ET) signatures whereas gray borders represent transpiration (T) isotope signatures. Treatment colors for all panels are indicated in **A**; however, the treatment lines with combined elevated CO_2 and warming are uniquely dashed in **A** to be more clearly distinguished from the warming treatment. The ^2H-labeled precipitation was added

to all treatments on 2021-08-02 (blue vertical line in **A**), marking the end of the experimental drought period; the vertical red bar in **A** represents a natural dry period following the label which ended with a rain event on 2021-09-15 just following the sampling period in **C**. Both **B** and **C** display δ^2H before and after the label was applied and are thus plotted with different y axis scales (inset vs general plot in **B** and left vs right panels in **C**). Data in **C** are displayed as boxplots where $n \geq 3$, and as points for $n < 3$, which are connected by a gray line where $n = 2$.

Fig. 2. Effects of water deficit on ecosystem water use. (**A**) Growing season cumulative precipitation minus evapotranspiration (P-ET) for the drought treatments in comparison to the ambient control (from SmartField Lysimeters (SFL)), (**B)** fraction of transpiration relative to total evapotranspiration via isotope mass balance (T/ET) displayed as boxplots where $n \geq 3$, and as points for $n < 3$, which are connected by a gray line where $n = 2$; and (**C**) transpiration tracer concentration normalized to the pre-label and label signature values and volume or normalized concentration curves (NC) (n = 3-6 per treatment and sampling event in **B** and **C**). Predictions in **C** represent a steady state advection-dispersion based Weibull model of water transport. Blue lines show the label timing (**A**), the yellow panel delineates the experimental drought period (**B**), vertical dashed lines denote periodic grassland cuts (**A**), and the vertical red bar in **A** and **C** represent a natural dry period following the label. Error bars in **c** represent the standard error of the mean. Treatment colors for all panels are indicated in **A**. Note that **A** includes only 3 of 6 treatments due to limited infrastructure and exclusion of erroneous SFL data.

Fig. 3. Soil water transport processes. (**A**) H1D-modeled cumulative transit time distribution of rootzone drainage at 36 cm per treatment, where diamonds denote median transit times. (**B**) H1D-modeled tracer curves versus soil pore volumes assuming either saturated or mean soil water content from the post-drought period (**C**). Treatment colors for both figures are indicated in **A**. The vertical red bar in **A** represents a natural dry period following the label. Error bands represent standard error of the mean pooled from all destructive soil δ^2H measurements taken across the rootzone for the monitoring period (n = 28-44 per treatment).

Fig. 4. Soil water mixing dynamics. 2021 post-drought (**A**) weekly ^{2}H signatures of precipitation and daily accumulation of precipitation and (**B**) volume-weighted pore water ^{2}H signatures (points) with mixing projections shown as lines which assume each precipitation event mixed completely with pre-event storage (i.e., approximating a "well-mixed" system). We additionally break down these comparisons per treatment in (**C**) with Kling–Gupta efficiency (KGE) estimates. Treatment colors for all figures are indicated in **A**. The ^{2}H-labeled precipitation was added to all treatments on 2021-08-02 (blue vertical line in **A**), marking the end of the drought or rainfall suppression period. Mixing projections were performed separately from our H1D analysis. The vertical red bar in **B** represents a natural dry period following the label event.

Fig. 5. **Conceptualizing rootzone hydrodynamics under global change**. **(A)** Illustration (and visual key for panels **D-L**) of how the labeled water (light to dark blue color ramp) moved through the soil-plant system, with particular attention to tracer position in pore space (soil "matrix" vs "macropore" guided by filled pore space vs pore size diagram; left-hand side of panel), the degree of pore water mixing (horizontal arrow), and how relevant water fluxes (evaporation, transpiration, and 60 cm seepage; vertical arrows) removed this water from the storage; here the red lines indicate from which part of the storage water was removed. Wavy horizontal lines delineate the soil A vs B horizon boundary (~30 cm), and large cavities networks

depict macropores filled with water signature (blue variation) or air (white); the exact distribution of macropore network is unknown and was chosen for illustrative purpose. **(B)** Illustration of annual wetting and drying cycles in the rootzone under climate manipulation (color coded by treatment). **(C)** Growing season cumulative precipitation minus evapotranspiration (P-ET) for the ambient [grey] and future [maroon] drought treatments in comparison to the ambient control [green] from SmartField Lysimeters where light blue lines show the label timing, yellow panel shows the experimental drought period, dashed lines show cuts, and the vertical red bar in **C** represents a natural dry period following the label. (**D**-**L**) Nine-panel illustration of the soil-plant system for the ambient (top row), ambient drought (middle row), and future drought (bottom row) treatments at three key time periods: after the label event (0-5 d; **D**-**E**), the peak of the natural dry period following the label (40-44 d; **G**-**I**), and the late season wet-up (44-70 d; **J**-**L**). Note, deep, air-filled macropores in **E** and **F** show that extremely dry pre-label conditions (lower water potential) in both drought treatments likely limited loss of labeled water via macropore flow by lateral reabsorption into the matrix. The grassland under recurring future drought is distinguished from other climate manipulations by its altered water use pattern, soil structure, and its ability to conduct water through larger macropores without mixing across the soil matrix.

Science
AAAS

Supplementary Materials for

Drought in a warmer, CO_2-rich climate restricts plant water use and soil water mixing

Jesse Radolinski[ab], Matevz Vremec[c], Herbert Wachter[a], Steffen Birk[c], Nicolas Brüggemann[d], Markus Herndl[e], Ansgar Kahmen[f], Daniel B. Nelson[f], Angelika Kübert[g], Andreas Schaumberger[e], Christine Stumpp[h], Maud Tissink[a], Christiane Werner[i], and Michael Bahn[a].

Correspondence to: jradolin@umd.edu

This PDF file includes:

Materials and Methods
Supplementary Text
Figs. S1 to S17
Tables S1 to S5
References (*66-123*)

Materials and Methods

Experimental site

The study site, ClimGrass (*35*), exposes a managed temperate, montane grassland to individual and combined (future) continuous, atmospheric warming and CO_2 enrichment following scenario RCP 6.0 (*37*), as well as recurring ambient and future drought. The study was conducted in 2021 following a long-term climate manipulation experimental site in the Enns Valley in northern Styria, Austria at an elevation of 707 m with a mean annual precipitation of 1009 mm and temperature of 8.5 °C (*60*). Since 2013, the facility has been managed by AREC Raumberg-Gumpenstein which has maintained replicated grassland plots (**Fig. S1**) with various combinations (*68*) of elevated CO_2, warming, and drought using a mini-FACE, or free air CO_2 enrichment system (*69*), infrared heating (*70, 71*) of the canopy air column, and automatic rain shelters (*35*) for the three global change factors, respectively. CO_2 enrichment was switched off daily during dark hours (evening to early morning) when global radiation was less than 50 W m^2. Annually, CO_2 enrichment was switched either off when the surface (at 10 cm) soil temperature was recorded to be less than 3°C at least once for five consecutive days in Autumn or switched on again in Spring when the threshold was exceeded for the same time period. Conversely, warming was only disrupted when snow cover exceeded 10 cm. Experimental droughts were imposed on the site during the growing seasons of 2017, 2019, 2020, and 2021 (**Table S1**). The grassland is dominated by C_3 grasses (*Arrhenatherum elatius, Dactylis glomerata,* and *Festuca rubra*) and forbs species (*Taraxacum officinale*, *Plantago lanceolata*, and *Lotus corniculatus*) and receives three cuts per year. Though less extensive as global C_4 grass distribution (*72*), C_3 grasses dominate cool-season regions (*73*). Roots are primarily distributed within 30 cm of the soil surface. Though significant increases have been observed in fine-root/shoot ratios for warming, there are no clear differences in root biomass or biomass distribution between treatments including, notably, in the future drought treatment. The site is underlain primarily by a *Cambisol* (Arenic, Humic) with a loamy sand texture and 2 distinguishable soil horizons: A (0-30 cm; very humic), and B (30-100 cm). Soil A and B horizons had a median saturated hydraulic conductivity of 114 cm d^{-1} and bulk density of 1.4 g cm^{-3}(*59*). See **Figure S1** for more site details.

Isotope measurements

We employed a variety of *in-situ* and destructive water stable isotope measurement techniques to build a comprehensive depiction of ecohydrological partitioning in and through the studied grassland across the 261-d monitoring period (May 7th 2021 to January 23rd 2022). Suction lysimeters (SK20, METER Group, Munich, Germany) were periodically sampled at 9, 18 and 60 cm depths (n = 3 per treatment and depth) under tension of 60 kPa for 3 h to study the isotope signatures of more mobile, liquid, water in the soil profile. Additionally, we used high resolution (4 h), state-of-the-art vapor monitoring of water stable isotopes in the soil profile to analyze bulk soil water isotope ratios at depths of 3, 9, 18, and 36 cm (n = 1 per treatment and depth). Briefly, this included a series of buried gas permeable membrane tubes (Accurel PPV8/2), which were multiplexed in a subsurface control structure (*35*) (**Figs. S15** and **S16**) to a cavity ringdown spectrometer (CRDS; L2130-i, Picarro, Santa Clara, CA) and flushed with periodic pulses of dry air using a Nafion drying unit (PD-50T-24MSS, Perma Pure LLC, Lakewood, New Jersey). We additionally conducted a series of chamber-based measurements (n =3-6 per treatment and measurement campaign) to determine the evapotranspiration and transpiration isotope signatures of our treatments. Evapotranspiration isotope signatures of vapor

were determined using a clear plexi-glass chamber (50 x 50 x 50 cm) positioned on a plastic frame over the grass canopy (*74*), equipped with fans to propagate turbulent mixing, and fitted with a teflon tube connection to a CRDS (L1102i, Picarro, Santa Clara, CA) which extracted a 30-40 mL min^{-1} subsample to analyze in real time. For transpiration isotope signatures we used a leaf chamber provided with the LiCor Li-6400 infrared gas analyzer (part no. 6400-05, LiCor Biosciences, Lincoln Nebraska) fitted to a CRDS (L1102i, Picarro, Santa Clara, CA) (*75*). Additionally, we used these estimates of soil, ET, and T isotope signatures to partition evapotranspiration into components of evaporation and transpiration (*76*). As an independent supplement to soil and transpiration isotope signatures, we collected periodic (2021-07-22, 2021-08-19, and 2021-10-13; n = 3-6 profiles per sampling time and treatment) destructive bulk soil water samples with high spatial resolution (5 cm and 10 cm intervals for 0-30 cm and 30-60 cm, respectively) and leaf tissue samples (n = 6-12 per treatment, and sampling time). These destructive samples were water-extracted via cryogenic vacuum distillation following Newberry et al. (*77*) and analyzed with a Thermal Conversion / Elemental Analyzer coupled to a Delta V Plus isotope ratio mass spectrometer (TCEA-IRMS) through a ConFlo IV interface (Thermo Fisher Scientific, Bremen, Germany). We describe details of the soil membrane tube system, chamber measurements, isotope analytical methodology and ET partitioning below.

Rainfall manipulation and labeling

We used automatic rainout shelters to suppress precipitation for treatments receiving experimental drought (ambient or with elevated CO_2 and warming) during the growing seasons of 2017 (-382 mm), 2019 (-161 mm), 2020 (-201 mm), and 2021(-295 mm). During these drought manipulation periods all other treatments were exposed to ambient precipitation. On the final day of each drought period, drought treatments received 40 mm of irrigation supplied from a reservoir of collected rainwater (Spring and Summer precipitation) and rainout shelters were then opened to terminate the drought. See **Table S1** for more details.

In the 2021 season, however, we extended this artificial rainfall application to all treatments using 40 mm of collected rainfall with an enriched δ^2H value of 3348 ± 178.3 ‰, distributed as two pulses of 20 mm at an average rate of 75 mm h^{-1}. The rainfall event was applied across the plots with a metered handheld sprinkler and periodically interrupted to prevent runoff. The standard deviation of this labeled water (~ 5% or ± 178.3 ‰ δ^2H) from 12 randomly collected samples of the applied water, suggests a relatively homogenous application of the label. Additionally, we used conservative numerical projections of soil water infiltration to show that overland flow was likely negligible during rainfall manipulations (**Fig. S16**), even without manual runoff restriction. The intensively monitored period of the label experiment fell between the site's second and third annual biomass cuts. The 2021 average cumulative P- ET_o (i.e., ambient P minus reference ET from start of growing season) between cuts 2 and 3 was 154 mm, which is within 23 mm or 17% of the site's 10-year median (130 mm; 2013-2022). The 10-year P- ET_o also indicates that this growth period (cuts 2-3; 130 mm) is typically much wetter than between cuts 1-2 (38.9 mm) and the start of growing season through cut 1 (-2.56 mm). Thus, the wetter label period was both 1) ideal for depicting changes to soil water transport under climate manipulation, and 2) phenologically and hydrologically relevant to the site's history.

Hydrological measurements

The ClimGrass facility is equipped with capacitive soil moisture sensors (Delta-T SM150, METER Group, Munich, Germany) and thermocouples (TCAV, Campbell Scientific,

Logan, Utah) at depths of 3, 9, 18, and 36 cm (n = 2 profiles per treatment). We scaled 15 min soil volumetric water content data from the four depths to weighted daily values across the soil profile. For **Fig. 1A**, θ values are comprised of a daily weighted average across the 4 depths using each respective measurement as representative of the spatial interval between them i.e., equal to θ_{3cm} x (3/36) + θ_{9cm} x (6/36) + θ_{18cm} x (9/36) + θ_{36cm} x (18/36). Four of the six treatments (ambient, ambient drought, elevated CO_2, and warming, and elevated CO_2 and warming with drought) were also equipped with a high precision weighable Smart Field Lysimeter (SFL-600, METER Group, Munich, Germany) or SFL's with dimensions of 707 cm^2 x 60 cm and filled with an intact monolith of study site soil. Malfunctioning of the SFL exposed to combined elevated CO_2 and warming prevented its use in this study. Additionally, the site contains six large weighable lysimeters (100 cm^2 x 140 cm; (*78, 79*) METER Group, Munich, Germany) or LL's comprising the Lysi-T-FACE concept (*71*) which span ambient, warming, and combined elevated CO_2 and warming treatments (**Fig. S1**)— providing long-term long-term water balance records (*79*). Though this study primarily uses SFLs for water balance records due to their scale-relevance to the rootzone, LL's provided supplementary water balance information for treatments not covered by the SFLs (**Fig. S3**). SFL's and LL's were used to precisely (± 10 g or 0.01 cm) monitor water balance parameters. High resolution (1 min) weight records were scaled to daily values using an adaptive window and adaptive threshold (AWAT) approach for excluding mechanical interferences (*80*). Precipitation measurements (1 h) were recorded via rain gauge at the site, and plant canopy level air temperature and relative humidity are recorded at 15 min resolution. In addition to these continuous hydrological measurements, we collected soil cores (5 cm x 5 cm) and unconsolidated material from the A (5-10 cm, representing 0-30 cm) and B horizons (35-40 cm, representing 30-100 cm) in the Autumn of 2019, and 2021 (n = 3-16 per treatment, depth, and time). We used a HYPROP 2 device (METER Group, Munich, Germany) to determine the soil field capacity (soil water content at matric potential -330 cm) and porosity (soil water content at matric potential at 0 cm) from these cores. Data from both soil sampling campaigns were pooled to provide an overall approximation of soil macroporosity (**Fig. S12**). The unconsolidated soil samples were used to quantify soil organic carbon content (SOC) via dry combustion with a Vario MAX CN macro elemental analyzer (Elementar, Hanau, Germany). In addition, leaf area index is estimated periodically using an AccuPAr LP-80 (METER Group, Munich, Germany) to aid in estimation of potential evapotranspiration at the site (*59*). More details regarding hydrological measurements are found at the end of the Materials and Methods.

Modeling of drainage fluxes

We derived soil water flux information for all 6 treatments by calibrating H1D to high resolution soil water content and stable isotope δ^2H values (3, 9, 18, and 36 cm) aggregated to daily time steps. To fully leverage the available observational data across both wet and dry periods and insure more robust model outputs, the entire available period was used for calibration rather than validating for prediction outside of our observational window (*81*). We used a modified version of H1D by Stumpp et al. (*82*) to model transient solute transport. This method removes effects of tracer evapo-concentration at the upper boundary and neglects isotope fractionation processes, which are indeed irrelevant under highly enriched values of δ^2H. H1D numerically solves the Richards equation for saturated-unsaturated water flow, which includes a sink term to account for root water uptake by plant roots (*83*):

$$\frac{\partial \theta(h)}{\partial t} = \frac{\partial}{\partial z}\left[K(h)\left(\frac{\partial h}{\partial z} + 1\right)\right] - S(z,h) \quad (1)$$

where θ is volumetric water content [$cm^3\ cm^{-3}$], h is soil water pressure head [cm], $K(h)$ is unsaturated hydraulic conductivity [$cm\ d^{-1}$], t is time [d], z is soil depth [cm] and S is a sink term due to root water uptake [$cm^3\ cm^{-3}\ d^{-1}$]. The Mualem-van Genuchten model (*84*) was used to describe the soil water retention curve $\theta(h)$ and hydraulic conductivity function $K(h)$. Here, the residual (θ_r) and the saturated water content (θ_s), the empirical parameters n [-], α [cm^{-1}], and saturated hydraulic conductivity (K_s) define the shape of these functions.

The upper boundary of the model domain was defined as a time-dependent atmospheric boundary with a surface layer, while the bottom boundary condition was defined as free drainage. Upper boundary inputs were daily precipitation measured at the site, potential evapotranspiration, and site-measured leaf area index data (AccuPAR LP-80, METER Group, Munich, Germany) to simulate crop growth and management. Although H1D does not include explicit photosynthetic processes, we considered the effects of elevated CO_2 on stomatal resistance and warming in the potential evapotranspiration estimation through adjustments in the Penman-Monteith equation (*59*). Input ET was then partitioned to potential soil evaporation and potential root water uptake using the Beers's law and leaf area index (*85*). The Feddes function (*86*) was used to model root water uptake which reduces the potential to actual root water uptake under dry conditions with water stress and under extremely wet conditions with a lack of aeration. We assumed that potential root water uptake from the 0-30 cm depth is linearly distributed, as proposed by (*87*). Snow accumulation and melting were modeled according to (*88*), using a snow melting and sublimation constant set to 0.43 [$cm\ d^{-1}\ °C^{-1}$] and 0.06 [-], respectively. Based on previous field soil characterization campaigns, two soil layers were considered: 0-30 cm and 30-140 cm.

The transport of the isotope label in H1D was based on a uniform convection-dispersion equation:

$$\frac{\partial(\theta C)}{\partial t} = \frac{\partial}{\partial z}\left(\theta D \frac{\partial C}{\partial z}\right) - \frac{\partial(qC)}{\partial z} \quad (2)$$

where C is isotope label concentration, q is vertical water flux, and D is dispersion coefficient that is defined for one-dimensional transport (*89*):

$$D = \frac{\lambda_L q}{\theta} + D_w \tau_w \quad (3)$$

where λ_L is longitudinal dispersivity [cm], $D_w$is molecular diffusion coefficient in free water [$cm\ d^{-1}$], and $\tau_w$is a tortuosity factor for the unsaturated zone. In the given case, the first term, which describes mechanical dispersion, is much larger than the second term, i.e. the effect of molecular diffusion can be neglected. Accurate depiction of the drought treatment combined with elevated CO_2 and warming, however, required the use of a dual-domain model framework which allows for limited exchange between matrix and macropores (see Supplementary Materials).

One set of optimal soil hydraulic properties and longitudinal dispersivity for two layers in each treatment was obtained by inverse modeling using soil water content and the isotope label concentration at 3, 9, 18, and 36 cm. This was done by employing the DREAM (DiffeRential Evolution Adaptive Metropolis) global optimization algorithm, described by Vrugt (*90*) and implemented in the Spotpy package. The data likelihood was taken as the average of pseudo-log-likelihoods (LogL) presented by Liu et al. (*91*) which uses a gamma distribution (w) and Kling-Gupta Efficiency (KGE):

$$LogL = \frac{n}{2} log \sum_{I=1}^{m} wf(1 - KGE) \quad (4)$$

where, n is the number of observations; $f()$ is the the gamma distribution function; m and w are the objective variables and weight assigned to each of them, respectively.

Tracer transport through plants and soil water mixing projections

We fitted a Weibull distribution function to post-label transpiration δ^2H data from all six treatments to determine the extent to which plant extraction of labeled water followed uniform, steady-state, advection dispersion transport (see **Fig. 2C**). The Weibull function has been shown to approximate advective-dispersive transport in shallow soils where dispersion is relatively strong (*41*). Thus, deviation from these distributions served as a first indicator of non-ideal tracer behavior in plant water use.

To understand how global change scenarios impacted soil water mixing across the rootzone, we compared our membrane tube δ^2H measurements to a series of conservative mixing projections across the monitoring period (see **Fig. 4**). We defined a running, per-treatment mixing projection as:

$$C_{mix} = C_s \frac{\theta_{pre-event} L_s}{\theta_{post-event}} + C_p \frac{P_{event}}{\theta_{post-event}} \quad (5)$$

where C_{mix} is the daily label composition (δ^2H in ‰) of the rootzone pore water, assuming that incoming precipitation— using accumulation (P_{event}) and its label composition (C_p) – combined with weighted pre-event soil water— using profile weighted average water content ($\theta_{pre-event}$) and label composition (C_s)— to produce a well-mixed post-event storage of ($\theta_{post-event} = \theta_{pre-event} L_s + P_{event}$) at the soil length scale L_s = 36 cm. C_s was set to the measured soil 0-36 cm weighted average δ^2H for the first time step and then subsequent values were set equal to the running mixing projection C_{mix}. When precipitation was absent, the mixing projection was set equal to C_{mix} from the previous day.

Statistical analysis

We statistically compared ET and T isotope signatures, and the fraction of T/ET for four key periods: two campaigns of intense drought (2021-07-08 and 2021-07-22), the period of highest recorded tracer signatures (2021-08-08), and the natural dry period (2021-09-15). Statistical comparisons were also made for isotope signature differences between suction lysimeter and membrane tube measurements which pooled data for the last three measurement

periods (2021-10-07, 2021-10-14, and 2021-11-02), and for soil readily drainable pore volume and SOC which pooled measurements from 2019 and 2021. All data were rank transformed on a per-sampling event basis upon failing normality tests via normal quantile plots or homogeneity of variance via Fligner's test, otherwise raw values were used. Comparisons were then made between treatments using a one-way analysis of variance (ANOVA) in R version 3.6.3 with Tukey HSD for post hoc analysis, and an overall significance level of $\alpha = 0.05$. Kling–Gupta efficiency (KGE) was used to assess hydrological model performance which scales Pearson's correlation by observed and simulated variances. KGE ranges from -0.41 to 1 where negative values represent models which fail to accurately predict mean observations and KGE = 1 represents perfect agreement between observed and simulated values.

Details of destructive soil, plant, precipitation, and in situ suction lysimeter water isotopic measurements

Destructive soil and leaf tissue samples and *in-situ* suction lysimeter were placed into 12 mL exetainer vials, sealed, and stored at -20 ℃ until cryogenic extraction and TCEA-IRMS analysis (*77*) . Leaf tissue samples consisted of 4 dominant species per plot replicate and sampling period including two grasses (*Arrhenatherum elatius* and *Dactylis glomerata*) and two forbs (*Plantago lanceolata* and *Taraxacum officinale*). Soil samples consisted of loose, homogenized material from the depth distribution described in Methods. All liquid water samples were normalized measurement runs to the VSMOW scale with in house standards producing analytical precisions of 0.68 ‰ δ^2H and 0.078 ‰ $\delta^{18}O$ across labeled natural abundance periods.

Details of continuous in situ soil water stable isotopic measurements

Stable isotope analysis of soil water vapor was performed in a remote monitoring system shown in **Fig. S15.** The membrane tube system cycled between combinations of six treatments and four depths on a four-hourly basis. During this 10-min sampling periods, sample air from 1 m vapor membrane tubes was cycled through our depth module and multiplexed in the analyzer interface at an average flow rate of 200 mL min^{-1} and subsampled by the Picarro for stable isotope analysis at 30-40 mL min^{-1}.

Our 1 m sample line length was 5-10x that of typical *in-situ* operations, (*92-94*) which integrated a larger, more representative, sample along the soil profile and reduced the effective time require to reach isotopic equilibrium during sampling events. However, this also presented a challenge for remotely sampling without condensation forming in the sample lines. Condensation in the sample lines is subject to Rayleigh fractionation and thus may not be representative of the soil profile water and can even interfere with or damage the CRDS optical cavity. Thus, we devised multiple means to safeguard against condensation interference. We first installed a droplet trap just downstream of the sample lines equipped with a capacitive sensor to detect accumulation of liquid water in the sample lines and notify handlers for removal. Our Reverse Drying Module (**Fig. S15**) described in the Methods section, could then be remotely activated to reverse flow and send dry (300-500 ppmv H_2O) air back to the membrane tubes after a water droplet alert. In addition, this drying system was run for 2 h every night to remove any residual condensation in the system. To further protect the CRDS analyzer form condensation,

we cycled a Drierite-dried (Drierite, Xenia, OH) volume of air through the analyzer cavity using a Picarro Standards Delivery Module or SDM (A101, Picarro, Santa Clara, CA).

We extracted the final 1 min (at 1 s resolution) of vapor sampling intervals as a representative measurement under thermodynamic (fluctuations ≤ 200 ppmv H_2O) and isotopic (≤ 2 ‰ and ≤ 0.5 for δ^2H and $\delta^{18}O$, respectively) equilibrium. We then removed sampling periods with extremely high (≥65000 ppmv) or low (≤ 5000 ppmv) absolute moisture values. These criteria helped to greatly reduce the possibility of condensation interference in the data. However, to avoid any remaining condensation issues, we removed suspicious sampling intervals upon visual inspection based on recommendations by Beyer et al. (*95*). For this modern CRDS analyzer, we found no significant water concentration-dependency in the measured stable isotope values, thus a concentration-dependency curve was excluded. Raw vapor phase stable isotope signatures were then converted to liquid phase based on *in-situ*, depth-specific soil temperature using standard equations by Horita and Wesolowski (*96*) to derive temperature-specific equilibrium fractionation factors. We then tested for sensor drift using consistent standards for δ^2H and $\delta^{18}O$. After detecting significant drift through time ($p < 0.05$) for ^{18}O during the post-label period, we applied a drift correction for this isotopologue and period based on recommendations by van Geldern and Barth (*97*). ^2H drift, however, was not significant. We then used 17 calibration periods of SDM standards with an average vapor concentration of 22100 ppmv to normalize data to the VSMOW scale with analytical precisions of 0.79 ‰ δ^2H and 0.27 ‰ $\delta^{18}O$ across labeled and natural abundance periods. These standards included values of -95.68, 1.8, 1.2, and 475.9 ‰ δ^2H and -13.46, 0.3, -1.97, and -7.13 ‰ $\delta^{18}O$ used in various combinations across the measurement period. Because we noticed a systematic offset from the local meteoric water line (LWML), we applied a simple offset correction for membrane tube data per isotopologue, treatment, and depth based on cryogenically extracted soil water values (**Fig. S15**).

Details of water stable isotope evaporation and transpiration measurements

For ET vapor isotope determination, we sealed the clear chamber described in Methods to a fiberglass frame for 2-5 minutes per plot whereby another CRDS analyzer (L1102i, Picarro, Santa Clara, CA) continuously sampled vapor from the chamber. From this period, we extracted the resulting 1-2 minute linear section of the measured saturation curve and derived the ET signature via Keeling method [*Keeling*, 1958] adapted for stable isotope mixing Walker and Brunel (*98*):

$$\delta_{bulk} = \left(\delta_{bg} - \delta_{ET}\right)\frac{C_{bg}}{C_{bulk}} + \delta_{ET} \quad \text{(S1)}$$

where δ [‰] and C [M L^{-3}] represent the stable isotope signature or water vapor concentration of the background (bg) or the mixture ("bulk") of ET and background air. Thus δ_{ET} was taken as the slope of the linear model relating the reciprocal of CRDS sampled air C_{bulk} to its isotope signature δ_{bulk}. Here we assume that the average background stable isotope stable signature remained constant over the measurement interval. To test this assumption, we maintained a 1-2 min pre-measurement of background air 1.2 m above the soil surface for all ET and T chamber measurements outside of the plot area. Relatively low standard deviations of background air δ^2H (1.72), $\delta^{18}O$ (0.36), and water concentrations (350 mg cm^{-3} H_2O), suggest that this assumption was reasonable. δ_{ET} values were accepted when statistically significant linear trends ($p \leq 0.05$) also had a coefficient of determination, R^2, greater than 0.7.

We measured transpiration isotope signatures using a modified approach outlined by Wang et al. (*99*) which consisted of a CRDS–connected, transparent leaf chamber attached to a representative mixture of plant leaves within the measurement frame for 2-5 min. Under steady state assumptions the transpiration isotope signature can be derived as:

$$\delta_T = \frac{C_{mix}\delta_{mix} - C_{amb}\delta_{amb}}{C_{mix} - C_{amb}} \quad \text{(S2)}$$

where the stable isotope signature of transpiration δ_T is unmixed from endmembers of ambient air measured at 1.2 m above plots and mixture vapor (subscripts "amb" and "mix," respectively). All ET and T measurements targeted mid-day or peak light intensity to maintain steady state assumptions at the leaf surface.

For post-processing of ET and T chamber measurements, we first applied an instrument-specific concentration dependency correction to measured δ vapor values via methods described in Schmidt et al. (*100*). We then tested for and found no significant drift for both isotopologues. We built standards curves on a per-measurement day basis from sampling campaigns where the CRDS analyzer sampled vapor headspace (30-40 mL min^{-1}) above liquid water in an 800 mL glass jar capped and fitted with an ambient air inlet valve connected to a Dierite canister. We extracted 1-2 minutes of standard vapor measurements in thermodynamic equilibrium fluctuations ≤ 200 ppmv H_2O) and isotopic (≤ 2 ‰ and ≤ 0.5 for δ^2H and $\delta^{18}O$, respectively). Measured standard vapor isotope signatures were fitted against temperature-specific, vapor conversions from standard liquid values of -73.16, 1.2, and 475.9 ‰ δ^2H and -8.48, -1.97, and -7.13 ‰ $\delta^{18}O$. We used these standard curves to normalize vapor measurements to VSMOW with an overall analytical precision of 0.69 ‰ δ^2H and 0.24 ‰ $\delta^{18}O$ across labeled and natural abundance periods. Chamber vapor values from the field were then finally converted to liquid based on per-measurement, mid-canopy air temperature records.

Partitioning evapotranspiration

We partitioned evapotranspiration into transpiration and evaporation components using an isotope mixing model:

$$f_{T/ET} = \frac{q_T}{q_{ET}} = \frac{\delta_{ET} - \delta_E}{\delta_T - \delta_E} \quad \text{(S3)}$$

which gives the fraction of transpiration q_T [M L^{-2} T^{-1}] relative to the aggregate evapotranspiration q_{ET} [M L^{-2} T^{-1}] flux, $f_{T/ET}$ [-] as a function of transpiration (δ_T), evapotranspiration (δ_{ET}), and soil evaporation (δ_E) isotope signatures. After deriving T and ET isotope signatures from chamber measurements we used a variation (*101*, *102*) of the Craig Gordon model (*103*) to estimate δ_E. This method adds to the original theory of Craig and Gordon (*103*), which combines effects of equilibrium and kinetic fractionation as liquid soil water evaporates, by accounting for the soil moisture contribution to relative humidity and vapor transport within the kinetic fractionation factor term, ε_k[-]. We calculated δ_E as:

$$\delta_E = \frac{\frac{\delta_S}{\alpha_{eq}} - RH_{bulk*}\,\delta_{bulk} - \varepsilon_k - \varepsilon_{eq}}{1 - RH_{bulk} + \varepsilon_{eq}} \quad \text{(S4)}$$

where the equilibrium fractionation factor α_{eq}[-] is equal to 1-ε_{eq} and ε_{eq} = (α_{eq} -1) x 10^3 is derived from liquid to vapor equilibrium calculations in Horita and Wesolowski (*96*), Horita and

677 Wesolowski (*104*). RH_{bulk*} [%] is the relative humidity for bulk air (ET combined with
678 background air) RH_{bulk} normalized to soil temperature using the empirical formulation (*105*) of
679 the Tetens equation (*106*):

680 $$RH_{bulk*} = RH_{bulk}\, e^{\left(\frac{17.502\,T_{bulk} - 17.502\,T_s}{240.97 + T_{bulk} - 240.97 + T_s}\right)} \quad \text{(S5).}$$

681 The subscript "s" denotes soil temperature and isotope signatures from 3 cm membrane tube
682 data—assumed to be representative of the evaporation front depth. The kinetic isotope
683 fractionation factor, ε_k was estimated as:

684 $$\varepsilon_k = (1 - RH_{bulk*})w\,[1 - \left(\frac{D_i}{D}\right)]^n \quad \text{(S6)}$$

685 whereby the boundary layer weighting term, *w*, was set to unity to denote no disturbances by the
686 evaporation flux, and $\frac{D_i}{D}$is the diffusivity ratio of water isotopologues along the laminar water
687 layer above liquid-vapor interface (0.9755 and 0.9723 for ^{2}H and ^{18}O, respectively) (*107, 108*).
688 The aerodynamic term, *n*, describes the development of laminar flow above the interface as a
689 function of soil water content (*109*):

690 $$n = \frac{0.5(\theta - \theta_{res}) + (\theta_s - \theta_{res})}{(\theta_s - \theta_{res})} \quad \text{(S7)}$$

691 where θ is the soil water content at the time of measurement, and θ_{res}, are the residual (assumed
692 $\theta_{res} = 0$) and saturated water content ($\theta_s = 0.45$) values, respectively. To represent pre- and post-
693 labeled periods with equal precision, we performed all ET partitioning calculations on measured
694 δ^{18}O signatures, which remained under natural abundance range for the monitoring period.

695 Rainfall simulation details

696 To ensure that the deuterium label fully infiltrated into the soil profile (without
697 significant runoff), we used numerical simulations to design the application of water. Here we
698 conservatively assumed that the saturated hydraulic conductivity of the A horizon (0-30 cm) soil
699 was 300 cm d^{-1} K_s, and that the pre-simulation soil water content was 0.25 for the wettest and
700 0.10 for the driest soils. With this information, we applied the one dimensional Philip (*110*)
701 infiltration model:

702 $$i = \frac{1}{2}St^{-1/2} + A \quad \text{(S8)}$$

703 where the infiltration rate *i* [L T^{-1}] is a function of the square root of time, a capillary force term,
704 sorptivity or *S* [L T$^{-0.5}$], and gravitational term, *A* [L T^{-1}] and is related to the soil's hydraulic
705 conductivity. We estimated *S*, with Philip's sorptivity equation:

706 $$S^2 = A\,(\theta_f - \theta_i)\frac{\Lambda}{b} \quad \text{(S9)}$$

707 where θ_i [L^3 L^{-3}] and θ_f[L^3 L^{-3}] represent the initial and final water contents, b [-] is an empirical
708 shape term ($0.5 \leq b \leq \pi/4$), and the matrix flux potential, Λ [L^2 T^{-1}], is given as:

709 $$\Lambda = \int_{h_i}^{h_f} K(h)dh = \int_{\theta_i}^{\theta_f} D(\theta)d\theta \quad \text{(S10).}$$

710

711 Equation S10 states that the matrix flux potential is equivalent to either the integral of the soil
712 hydraulic conductivity function across the measurement range (i.e., initial to final) of matric
713 potential, *h* [L^2 T^{-1}], or soil diffusivity, *D* [L^2 T^{-1}] across the range of water contents during the

infiltration process. We chose to derive Λ using $K(h)$ with Van Genuchten's hydraulic conductivity function (*84*):

$$K(h) = K_s \frac{\left(1-(\alpha h)^{n-1}[1+(\alpha h)^n]^{-m}\right)^2}{[1+(\alpha h)^n]^{m/2}} \; ; \qquad m = 1 - \frac{1}{n} \tag{S11}$$

where K_s [L T^{-1}] is the saturated hydraulic conductivity, (assumed to be representative of the A horizon 300 cm d^{-1}), α [L^{-1}] is positive value related to the inverse of the soil's air entry pressure (assumed 0.06), and n [-] is an empirical shape parameter (assumed 1.2). Here we also used Van Genuchten's soil water retention function to determine the initial matric potential of the soil:

$$h(\theta) = \frac{(\frac{(\theta_r-\theta_s)^{\frac{1}{m}}}{\theta_r-\theta}-1)^{1/n}}{\alpha} \tag{S12}$$

using a saturated (θ_s) and residual θ_i water contents of, of 0.44 and zero, respectively. Note that all Van Genuchten parameters were laboratory-derived for the study site soil. Finally, we used a conservative estimate of $A = K_s/3$ recommended by (*111*) to complete the infiltration projection. Results, shown in **Fig. S17** show a negligibly small accumulation of ponded water during the rainfall simulations.

Details of hydrological monitoring

Site soil moisture records were assessed on an aggregate basis extending from 2014 to 2021. After technical filtering (θ values of 0-0.6), we referenced daily aggregated moisture values to periodic, independent TDR measurements taken during the 2015, 2016, and 2017 growing seasons. In situ sensors generally had a strong agreement with these periodic measurements. Those that did not (e.g., $r^2 < 0.5$); however, were flagged for potential sensor error.

We performed a QAQC procedure on 15 min resolution data following a standard protocol for soil moisture datasets by Dorigo et al. (*112*) . This included flagging potential periods where sensor error occurred such as plateaus, freezing, spikes, and breaks (spikes resulted in temporary or permanent offsets). First, values were excluded that extended beyond 0.6 or below zero. Data was then manually processed by removing any remaining periods of sensor failure.

To identify periods of potential sensor drift, we first estimated field capacity directly from soil moisture data using a modified algorithm from Bean et al. (*113*) at 1h resolution. We fit a linear model of field capacity estimates versus time to all sensor data to gauge the occurrence of sensor drift. We noticed that r^2 values greater than 0.3 corresponded to datasets whose values began drifting following a trigger event such as breaks where spikes result in temporary or permanent offsets. When applicable, these subsequent drift periods were removed following the trigger event. We then calibrated all values via linear offset from gravimetric soil moisture samples taken at the corresponding plot and sensor depth

Further experimental site details and drought characteristics

The ClimGrass facility is intended to provide concrete depictions of potential future climate alterations to montane grasslands through a long-term climate manipulation experiment, which started in 2014. A recent global meta-analysis of climate manipulation experiments (*23*), reported just 7 experiments worldwide which combine treatments of warming, CO_2 enrichment,

and drought manipulations. To the best of our knowledge, ClimGrass is the only facility world-wide to warming, CO_2 enrichment, and drought manipulations with high precision lysimetry in grasslands. Further, besides the current study, we know of no other study which uses multifactor global change observations to understand future mechanism of ecohydrological partitioning or water transport. Thus, we emphasize that this study represents a globally unique depiction of future vadose zone processes. **Fig. S1** shows an abbreviated schematic of the ClimGrass facility with relevant treatments and infrastructure.

Automatic rainout shelters were used to suppress rainfall for plots designated "C0T0D" or "C2T2D" (**Fig. S1**) for the years 2017, 2019, 2020, and 2021. These shelters use a sensitive pressure transducer to detect the first few raindrops from a precipitation event, and automatically enclose the structure in a UV-transparent plastic sheet. **Table S1** shows a summary of each simulated drought. On June 21, 2021, an intense thunderstorm ripped through the rainout shelter barriers, creating runoff inside these drought manipulation structures, and resulted in 30-40 mm of infiltration across the field site. However, a silicone barrier excluded infiltration directly within Smart Field Lysimeters. See "SFL water balance in the context of field measurements" below for clarifications between soil moisture records in the field versus SFL-derived water balance data.

Supplementary Text

Drought water transport comparison

We use this section to highlight the striking difference in subsurface transport characteristics that were observed between drought treatments (**Fig. S2**). These differences occurred despite slightly drier water contents observed in the ambient drought before the label (**Fig. 1**), and similar seepage events following the label (**Fig. S2**). Note that drainage in **Fig. 3** represents 200 d of modeled soil water flux at the lower rootzone (36 cm), while seepage in **Fig. S2 (**left side**)** is <100 d of measured free drainage at 60 cm. Because there is a high residual tracer in the future drought (ET removal is reduced), small increases in soil water flux translate to higher proportional tracer losses in drainage (**Fig. 3**). Additionally, intense drying in this system during (and even before; **Fig. S3**) means that the (likely air-filled) pore space between 36 and 60 cm may need to approach saturation to produce seepage. Thus, 36 cm drainage does not necessarily translate to analogous 60 cm seepage per-event. The strong reduction of labeled water for the ambient drought in **Fig. S2** (following the seepage event) may have resulted from redistribution of tracer from the rootzone (**Fig. S5**) to deeper in the soil profile (**Fig. 5K**), and potentially some displacement of matrix water into rapidly flowing macropores.

Reduced evapotranspiration during drought and post-label periods for future drought treatment

We further integrated SFL and LL data to show a per treatment and cut estimation of cumulative evapotranspiration during the 2021 growing season (**Fig. S3**). The future drought treatment displayed elevated ET relative to other treatments early in the growing season (first cut), but clearly reduced these evaporative losses during and after the drought (e.g., second and third cut). These results further support the assertion that tracer outflow may have been significantly limited for the future drought treatment.

Rootzone profiles

To get a more detailed understanding of soil water dynamics across the rootzone profile during the monitoring period, we show the spatial and temporal distribution of rootzone soil water and δ^2H under key experimental periods (**Fig. S5**). These periods include peak drought (2021-07-21 to 2021-07-30), the label event (incl. day before the label: 2021-08-02; and 2021-08-02 to 2021-08-10), natural dry period of intense soil water decline (2021-09-06 to 2021-09-15), and late season wet-up period (2021-10-05 to 2021-10-14). These data show more clearly how the deuterium label persisted across the soil profile for the future drought scenario. One striking detail is the difference between the two drought treatments from the label event period to the natural dry period. Whereas the difference between the tracer profile distributions is relatively minimal for the drought treatments during the label event period, we detected >2 fold higher label signatures at 18 cm for the future drought treatment during the natural dry period. More intense redistribution of the label water in the future drought treatment (lower rootzone decrease of δ^2H while upper rootzone decreases; **Fig. S5**) relative to other treatments during the natural dry period corresponds well with the observed increases transpiration δ^2H (**Figs. 1C**, and **2C**).

Details regarding antecedent soil moisture and macropore flow following the labeled rewetting

Soil macropores often will intersect the surface or be close enough to the surface (or the high porewater pressure of the wetting front) that these highly conductive pathways will trigger preferential transport of the event water. However, under low antecedent soil moisture significant macropore flow can be suppressed—such that macropore activation e.g., near the surface can be absorbed back into the matrix (*114*) at a lower depth due to the sharp water potential gradients across the profile. Under wetter initial conditions (e.g., non-drought treatments), this capillary inhibition of preferential flow is reduced (*115*), which can trigger more overall bypass flow (*47*). Thus, in both drought treatments, drainage losses of tracer after the initial labeling could have been substantially minimized, despite the existence of a macropore network. **Fig. 5E** and **5F** illustrate that water moving through macropores during the label event was pulled back into the dry soil matrix below the root zone for the two drought treatments.

Hydrological modeling results

Below we present the results of the H1D inverse model calibration procedure, including parameter descriptions (**Table S2**), as well as pre (**Table S3**) and post calibration (**Table S4**) parameter values. **Fig. S5** shows the H1D performance for all 6 treatment models. During calibration, the residual water content (θ_r) and the tortuosity factor (τ) were kept constant at 0.05 and 0.5, respectively.

Improved H1D model fit after reduced daily tracer removal by plants

We note here that the Hydrus 1D model simulations (details described in main text and below) were initially unable to accurately simulate isotopic tracer measurements for the future drought treatment ("+300 ppm CO_2 & + 3 ℃ (Drought)"). To address this limitation, we made several changes: 1) we modified the Feddes term for daily solute uptake (*Crootmax* = 150), to reduce the amount of tracer removed by plants following the label, and 2) we included a dual porosity system where the transfer between matrix and macropore domains is proportional to the effective saturation of the two regions. With less removal through evaporative fluxes, this allowed the system to accumulate higher tracer mass in the rootzone and better match observations throughout the post-label period while also creating more losses to drainage. Further, the dual porosity model configuration allowed for rapid periodic solute movement through the macropore domain while limiting interaction with the matrix. Altogether, the model simulations were greatly improved with these two mechanistic adjustments (**Fig. S6**). **Table S5** shows the final parameter estimates.

We believe that variability in modeled K_s (e.g., 0-30 cm; **Table S4**) reflects how the natural soil heterogeneity is amplified by each treatment, and how this variability propagated through a highly (hydrologically) variable calibration period of wet and dry periods. It's also important to note that it is not uncommon for experimental measurements of K_s to span >2 orders of magnitude at the field scale (*116, 117*). Additionally, the variability of modeled K_s in the B horizon is less extreme, likely due to the reduced total variation in water content during the calibration period.

Details regarding of water use during the natural dry period

All treatments accessed older (~45 days) tracer water during the natural dry period, but the differences in magnitude of tracer use are key to interpreting the relative ecohydrological responses. Though the tracer signature in transpiration was relatively high in the future drought treatment from the label period through the natural dry period, it remained similar in magnitude to other treatments (e.g., ambient drought and warming; **Figs. 1C**, **2C** and **5D-F**). We argue that this was driven by water availability and its impact on ecosystem water use. For example, the future drought had an exceptionally high retention and high label signature remaining in rootzone pore water before the natural dry period, yet the tracer response in transpiration—though high— was not substantially greater. This suggests that the plants may have preferentially removed a younger fraction of storage during this period, but the natural dry period reversed this preference. When the entire grassland rapidly removed soil moisture, all plants were forced to access slightly older storage in the finer pores of the soil matrix. During this key natural dry period, the future drought had a significantly higher label signature in transpiration relative to other treatments (**Fig. 1C** and **2C**)and was thus more effective at accessing this older storage compared to treatments (**Fig. 5G-I**).

Details regarding suction lysimeter and hydrological domain separation

We use this section to compare soil water isotope "bulk" signatures measured from the high resolution (n = 1 per treatment; 4 h resolution) in situ system versus the more mobile water periodically extracted from suction lysimeters (installed n = 3 replicated plots per treatment and soil depth) which integrate pore water from 0 to 60 kPa. **Fig. S8** shows the suction lysimeter water ^{2}H signatures (black borders) and the bulk values observed for the respective lysimeter sampling day (treatment color borders). The drought treatment with elevated CO_2 and warming generally shows the highest separation between the two hydrological domains (**Fig. S9**), and shows a separation that uniquely changes sign (barring the ambient drought on 2021-08-11, 9 cm, **Fig. S9**) after the day of the label or 2021-08-02.

Destructive soil and leaf water isotopic measurements compared to observed trends in membrane tubes and chambers

We compared replicated, destructive samples of soil (**Fig. S10**) and leaf (**Fig. S11**) water with soil membrane tube and chamber measurements, respectively, to determine whether our core isotopic measurements were representative of the entire field, throughout the study period. Destructive soil water samples followed the general per-treatment trend of water isotope transport observed in our high-resolution vapor membrane tube measurements (**Fig. S10**). Similarly, transpiration water isotope signatures align well with destructive leaf water isotope samples (**Fig. S11**).

Details regarding soil readily drainable porosity and macroporosity

A soil's porosity describes the amount of void space relative to the total soil volume, through which air and liquid can permeate. Under saturated conditions (matric potential of 0 cm or higher), the volumetric water content, θ, is roughly equal to this total void space, assuming complete displacement of air. A soil's field capacity is the water content at which free soil water drainage—according to gravitational forces— becomes negligibly small (*118*) or where the remaining soil water is held in pores under capillary forces (usually approximated at max. -330 cm (*119*)). Thus, the difference between porosity and field capacity depicts the pore space where water flow is most rapid and readily drainable (*120, 121*) —though not typically considered plant accessible. Encompassing the most conductive soil pores, this readily drainable pore volume has been used to approximate climate-induced alterations to soil macroporosity (*57, 121*). The future drought treatment had a higher readily drainable pore volume relative to other treatments, though this trend is much weaker in the near-surface, A horizon (**Fig. S12**). The clearest future drought effect on readily drainable pore volume can be seen in the B horizon where we detected the most extreme hydrological disconnections in pore space (e.g., 36 cm in **Fig. 1**). We recognize that it is also possible that drought-induce hydrophobicity (*122*) may have created "channeling" or confining water within preferential flow paths in the future drought system; however, we have little evidence to confirm. Further, the soil organic carbon content (SOC) in the B horizon of the future drought system had a slight trend of more organic carbon relative to other treatments. Though weaker than the readily drainable pore volume trend (ANOVA; $p > 0.05$), a direct comparison between elevated the B horizon SOC of the future drought versus its non-drought counterpart (combined elevated CO_2 and warming) still yielded a student's t test of $p = 0.03$. As mentioned in the main text, we speculate that more SOC in the B horizon of the future drought treatment may partially provide more organo-mineral complexation and a means to stabilize the macropores (*123*) in the relative to other climate manipulation scenarios. We note that we lack clear evidence for a mechanism underlying this small increase in SOC observed in the future drought treatment (median difference of 0.02 % SOC; future drought vs ambient; **Fig. S12**), also given that no clear treatment effects on root production were found (*124*). However, minor insignificant annual inputs from root turnover or root exudation as well as shifts in soil organic matter mineralization may have led to a small accumulation of SOC over multiple years.

Details regarding SFL water balance in the context of field measurements

Here we clarify discrepancies between data derived from lysimeter weights (e.g., P-ET; **Fig. 2A**) and those of the weighted soil water content in the rootzone (e.g., **Fig. 1A**). Namely, soil water content data in **Fig. 1A** depict a drier rootzone in ambient versus future drought conditions by the end of the drought period and include a response to one rainfall event during the drought manipulation period. These two responses are not directly reflected in the P-ET time series of drought treatments in (**Fig. 2A**), where P-ET is lower in the future versus the ambient drought treatment and does not respond to a mid-drought precipitation event.

As mentioned in the "Further experimental site details and drought characteristics" section of the Supplemental Materials, though the rest of the drought plots (and all other treatments) were directly exposed to this mid-season precipitation event, the SFLs under drought treatment remained unaffected. Thus, this mid-drought interruption is not directly reflected in the P-ET data in **Fig. 2a**. However, we accounted for these inputs in our H1D modeling exercise.

Though, it may be difficult to definitively say that the rootzone was substantially drier in either of the drought treatments during the 2021 drought, it is clear that: 1) both treatments had little soil water storage, and that 2) previous drought records (**Table S1**) and the P-ET from SFLs show that the grassland under future drought consistently produces a drier system. Further, the scales of the rootzone soil water measurements (0-36 cm) versus that of the lysimeter water balance measurements (0-60 cm) are important when interpreting both datasets. Assuming a porosity of 0.5, the SFL system records up to 120 mm (0.5 x 24 cm) more storage than the rootzone measurements. By the time the drought simulation began, the future drought started the drought period with > 100 mm lower P-ET than that of the ambient drought. Thus, much of the buffer storage of 120 could have been removed early into the drought. Given this information, one could even observe a slightly wetter future versus ambient drought conditions in the rootzone by the end of the drought, but still be at a greater water deficit at the 0-60 cm water balance scale. Lastly, our tracer data (e.g., **Figs. 1B**, **1C**, **S5**, **S8**, **S9**, **S10**, and **S11**)—which provide integrative information of flowpaths, and water pools, etc. — are consistent with both the point measurements in **Fig. 1A** and the water balance information in **Fig. 2A** and **S3**. Both the soil water measurements from the field and the SFL data are important for assessing the hydrological effects of climate manipulation.



Fig. S1. **Relevant infrastructure, plots, and treatments within the ClimGrass facility**. Treatments are comprised of various combinations of elevated atmospheric levels of CO_2 (ambient, +150, and +300 ppm are denoted by C0, C1 and C2) and air temperature (ambient, +1.5°, and +3°C; given as T0, T1 and T2), and recurring drought

959 conditions (denoted by “D” in treatment name) using automatic rainout shelters. The “Membrane tubes” label
960 identifies plots where soil water stable isotope signatures were monitored in situ in high resolution (4 h). The current
961 study considered the treatments: C0T0, C2T0, C0T2, C2T2, C0T0D, and C2T2D.

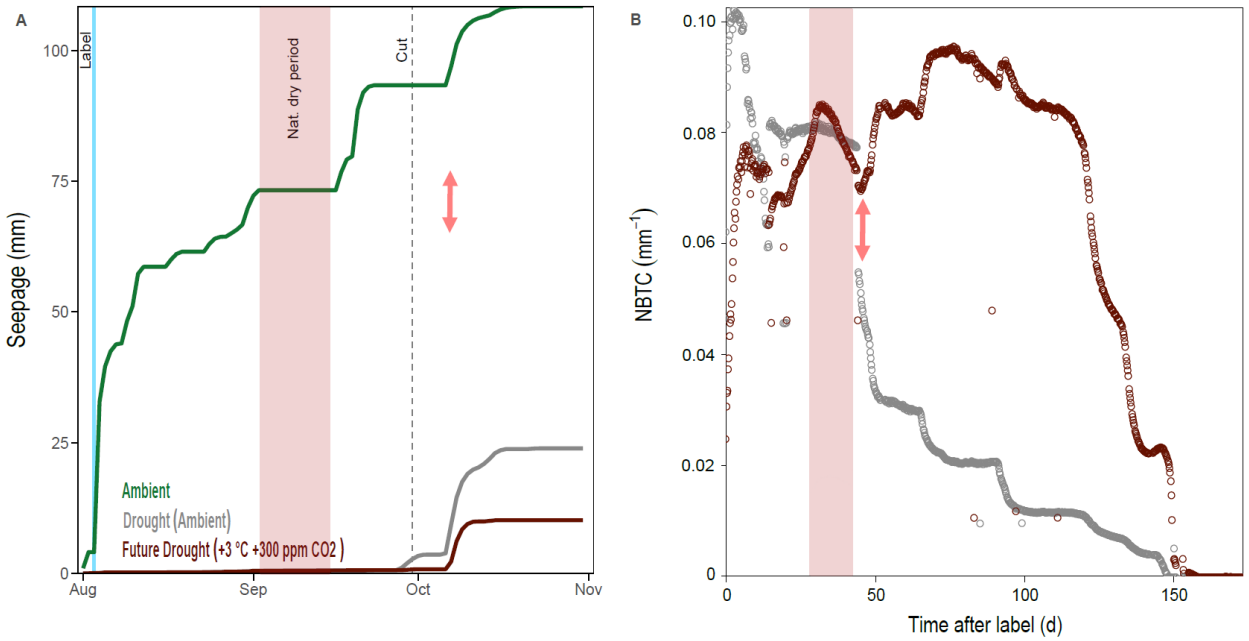


Fig. S2. Post-label seepage and normalized breakthrough curve of drought treatments. (**A**) Post-label cumulative seepage from Smart Field Lysimeters (SFL's) at 60 cm (n = 1 per treatment) and (**B**) stable isotope signature of 36 cm soil water (n = 1 per treatment) normalized to the pre-label and label signature and volume or normalized breakthrough concentration (NBTC) in dimensions of L^{-1}. Label was applied on August 2nd, 2021. Drought treatments are compared here to highlight extreme differences in water transport patterns despite both having similar post-label seepage. The red arrows highlight when both drought plots produce seepage in the post-label period. The vertical red bar represents a natural dry period following the label.

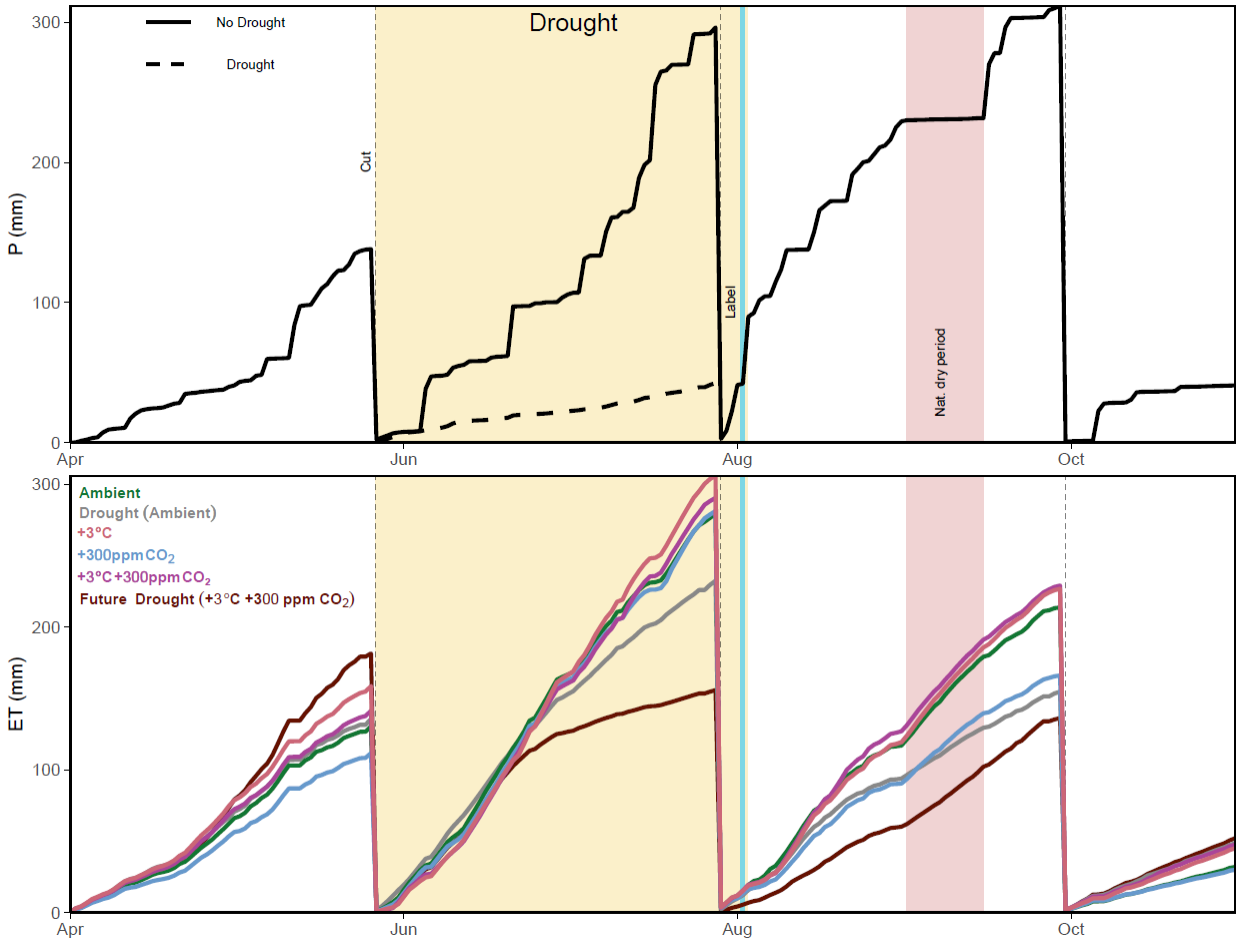


Fig. S3. 2021 Cumulative precipitation and evapotranspiration per grass cut period. (**A**) Cumulative precipitation (P) per cut (vertical dashed line) from "no drought" (average of ambient Smart Field Lysimeters—SFL's— and Large weighable Lysimeters—LL's) and "drought" (average ambient and future drought SFL's). (**B**) Cumulative evapotranspiration (ET) per cut and treatment; ambient, warming, and elevated CO_2 represent averages of $n = 2$ lysimeters. The yellow panel delineates the experimental drought period , the vertical red bar represents a natural dry period following the label, and dashed line indicates the last or third grassland cut of the season. Label was applied on August 2nd, 2021, marking the end of the experimental drought or rainfall suppression period (beige panels). Small, periodic increases in P during the drought (for drought treatments) represent non-rainfall water accumulation (e.g., dew formation). Comparisons begin on 2021-04-01 after brief malfunctioning of the LL system in March 2021.

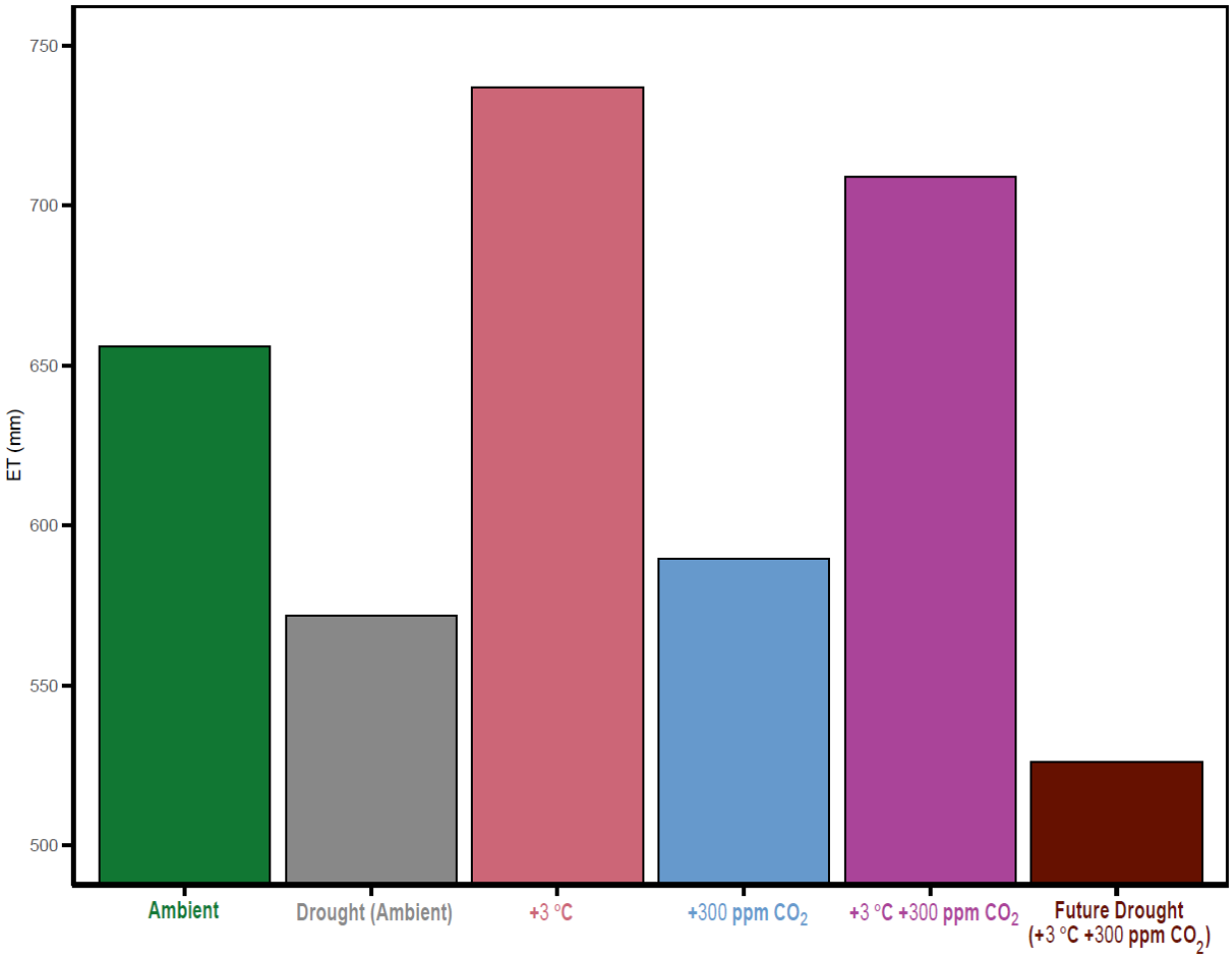


Figure S4. **Cumulative growing 2021 season evapotranspiration (ET)** derived from weighable lysimeters (SFLs and LLs; *n* = 1-2 per treatment).

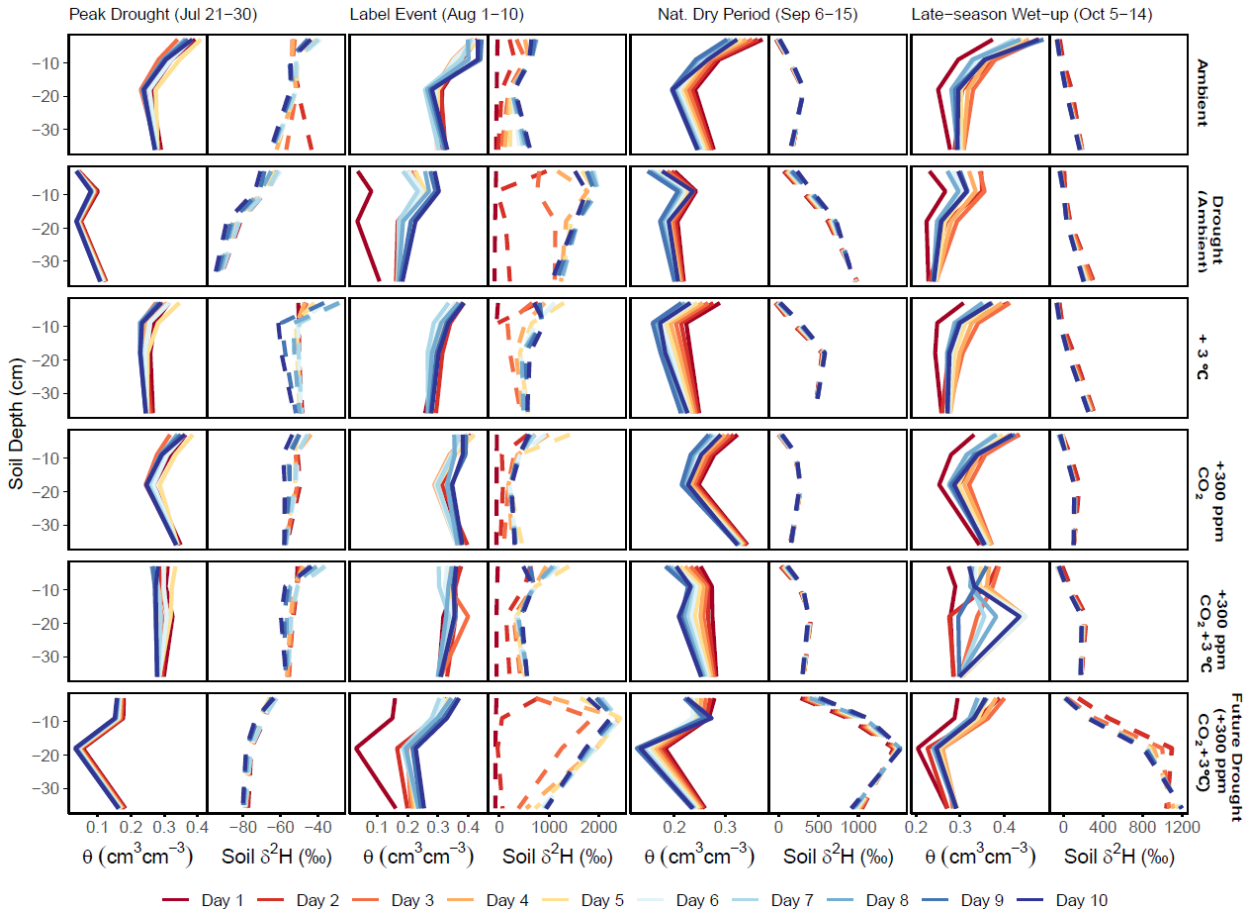
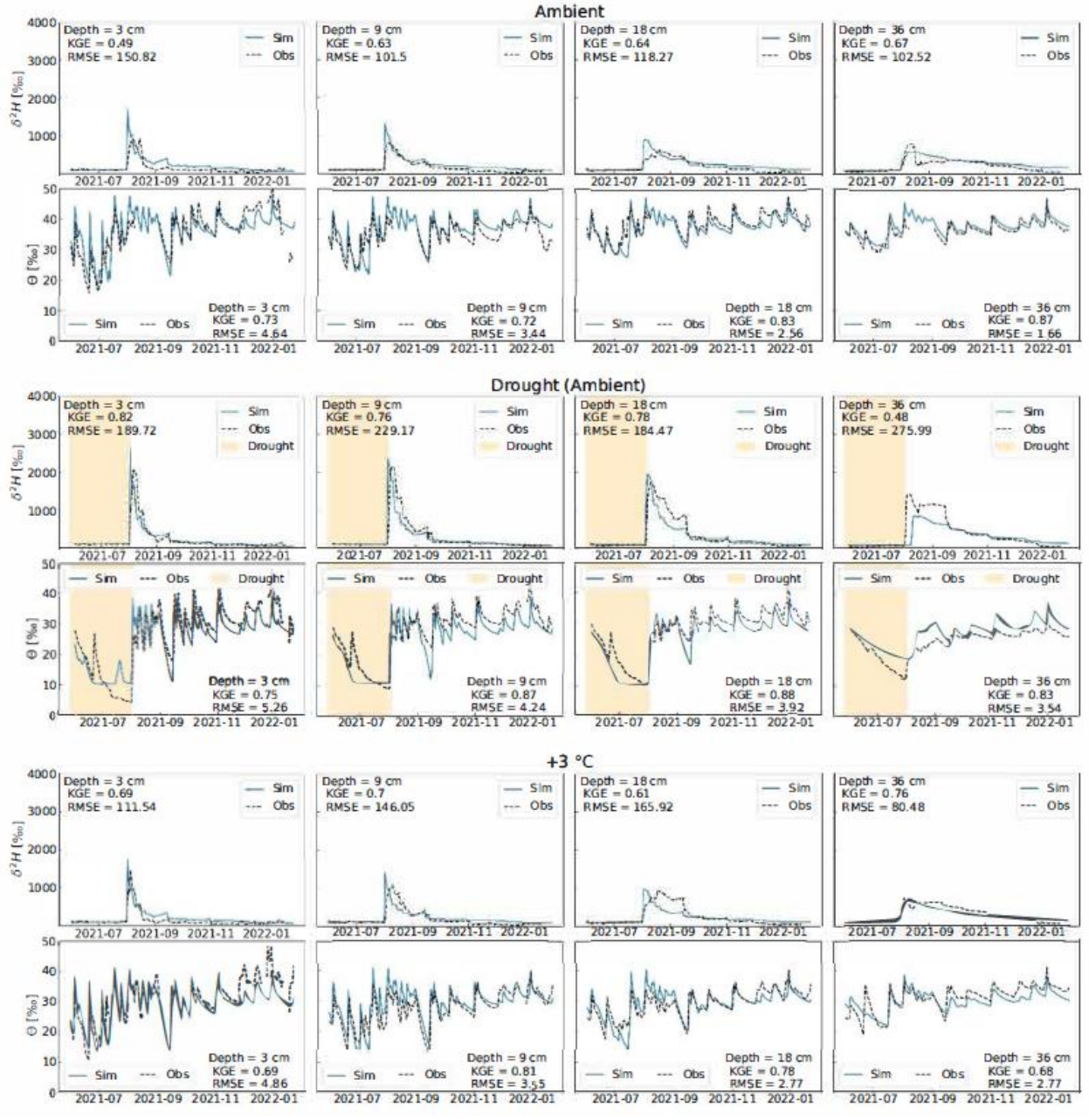


Fig. S5. Rootzone soil water and δ^2H profiles. Rootzone soil water profiles showing soil depth versus soil water content (θ; n = 2 per treatment; solid lines) and δ^2H measured from soil membrane tubes in water vapor (n = 1 per treatment and depth; dashed lines) for four key time periods: peak drought (2021-07-21 to 2021-07-30), the label event (incl. day before the label: 2021-08-02; and 2021-08-02 to 2021-08-10), natural dry period following the label (2021-09-06 to 2021-09-15), and late season wet-up period (2021-10-05 to 2021-10-14). The line color-ramps depict the beginning (red) to the end (blue) of each highlighted interval at a daily resolution.


Ambient
Depth = 3 cm
KGE = 0.49
RMSE = 150.82
Depth = 9 cm
KGE = 0.63
RMSE = 101.5
Depth = 18 cm
KGE = 0.64
RMSE = 118.27
Depth = 36 cm
KGE = 0.67
RMSE = 102.52
Sim
Obs
δ²H [‰]
Θ [‰]
2021-07 2021-09 2021-11 2022-01
Depth = 3 cm
KGE = 0.73
RMSE = 4.64
Depth = 9 cm
KGE = 0.72
RMSE = 3.44
Depth = 18 cm
KGE = 0.83
RMSE = 2.56
Depth = 36 cm
KGE = 0.87
RMSE = 1.66
Drought (Ambient)
Depth = 3 cm
KGE = 0.82
RMSE = 189.72
Depth = 9 cm
KGE = 0.76
RMSE = 229.17
Depth = 18 cm
KGE = 0.78
RMSE = 184.47
Depth = 36 cm
KGE = 0.48
RMSE = 275.99
Drought
Depth = 3 cm
KGE = 0.75
RMSE = 5.26
Depth = 9 cm
KGE = 0.87
RMSE = 4.24
Depth = 18 cm
KGE = 0.88
RMSE = 3.92
Depth = 36 cm
KGE = 0.83
RMSE = 3.54
+3 °C
Depth = 3 cm
KGE = 0.69
RMSE = 111.54
Depth = 9 cm
KGE = 0.7
RMSE = 146.05
Depth = 18 cm
KGE = 0.61
RMSE = 165.92
Depth = 36 cm
KGE = 0.76
RMSE = 80.48
Depth = 3 cm
KGE = 0.69
RMSE = 4.86
Depth = 9 cm
KGE = 0.81
RMSE = 3.55
Depth = 18 cm
KGE = 0.78
RMSE = 2.77
Depth = 36 cm
KGE = 0.68
RMSE = 2.77

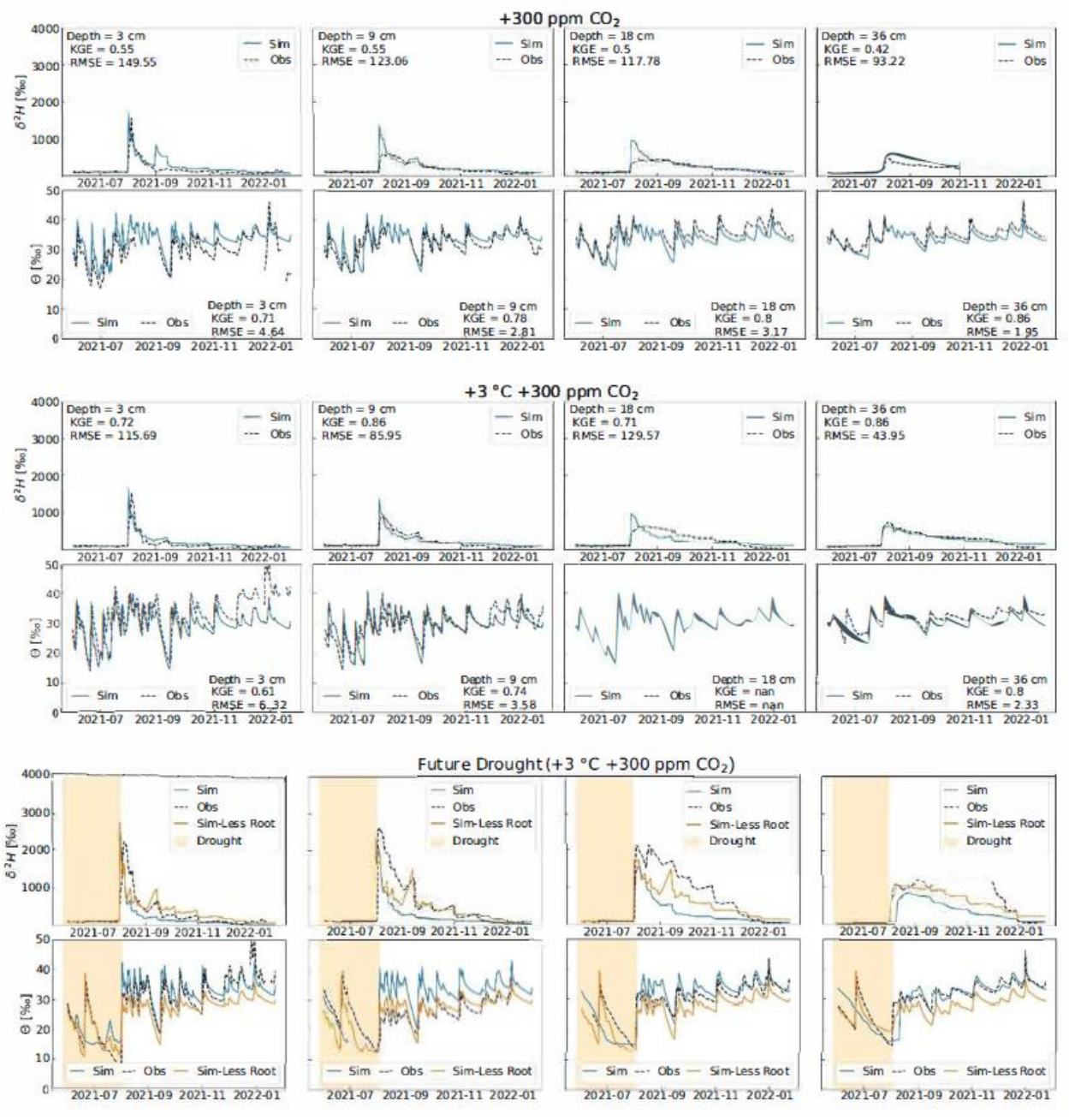


Fig. S6. **Fitted H1D results**. Observed ("Obs") and H1D simulation ("Sim") results for soil water content, θ, and soil δ^2H for H1D at 3, 9, 18, and 36 cm (i.e., the 4 columns). For the future drought treatment, "Sim-Less Root" denotes the improved simulations using reduced *Crootmax* and dual porosity. Yellow panels denote the experimental drought or rainfall suppression period.

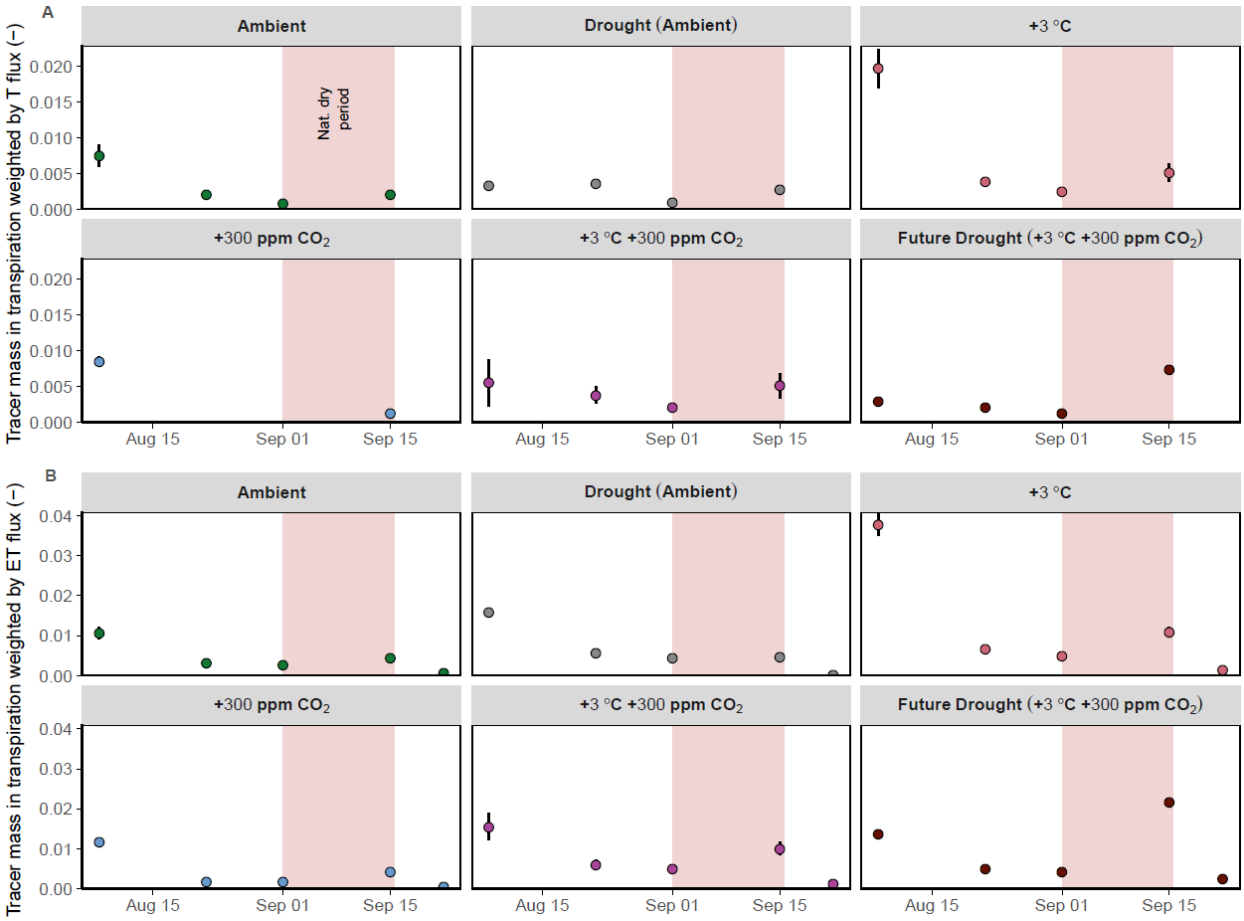


Fig. S7. **Daily relative tracer mass fraction loss in transpiration** weighted by transpiration (**A**) or ET flux (**B**). The vertical red bar represents a natural dry period following the label. Error bars in c represent the standard error of the mean.

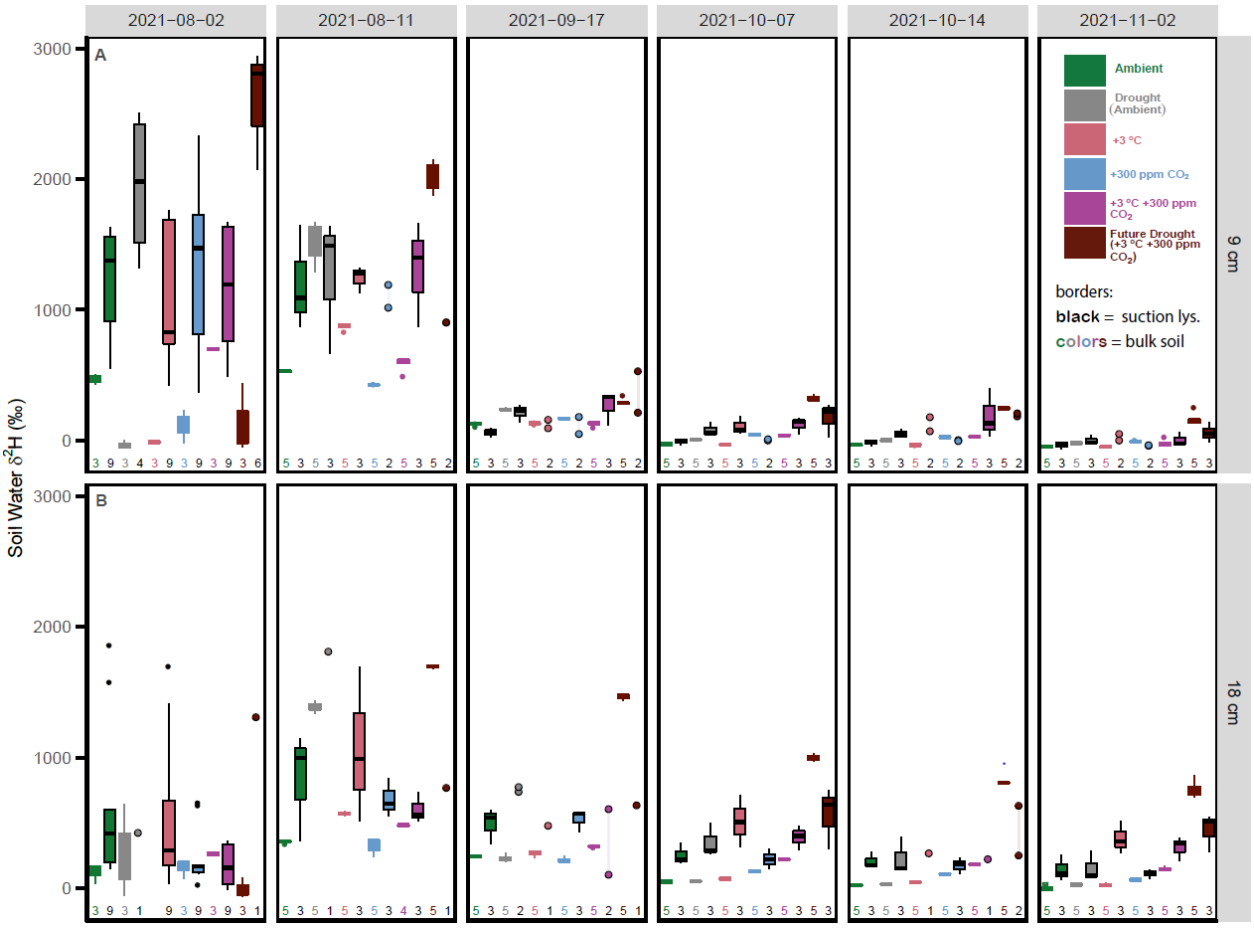


Fig. S8. **Post-label mobile suction lysimeter water δ^2H**. Soil stable isotope signatures from suction lysimeter (black borders) and bulk soil water from vapor membrane tubes observed for the respective lysimeter sampling day (treatment color borders) for 9 (**A**) and 18 (**B**) cm depths during the post-drought period across the six global change treatments. Numbers on panel floors display *n* observations per treatment, depth, and sampling day (suction lysimeter $n > 3$ reflect x3, 2-h resolution sampling during label). Data are displayed as boxplots where $n \geq 3$, and as points for $n < 3$, which are connected by a line where $n = 2$.

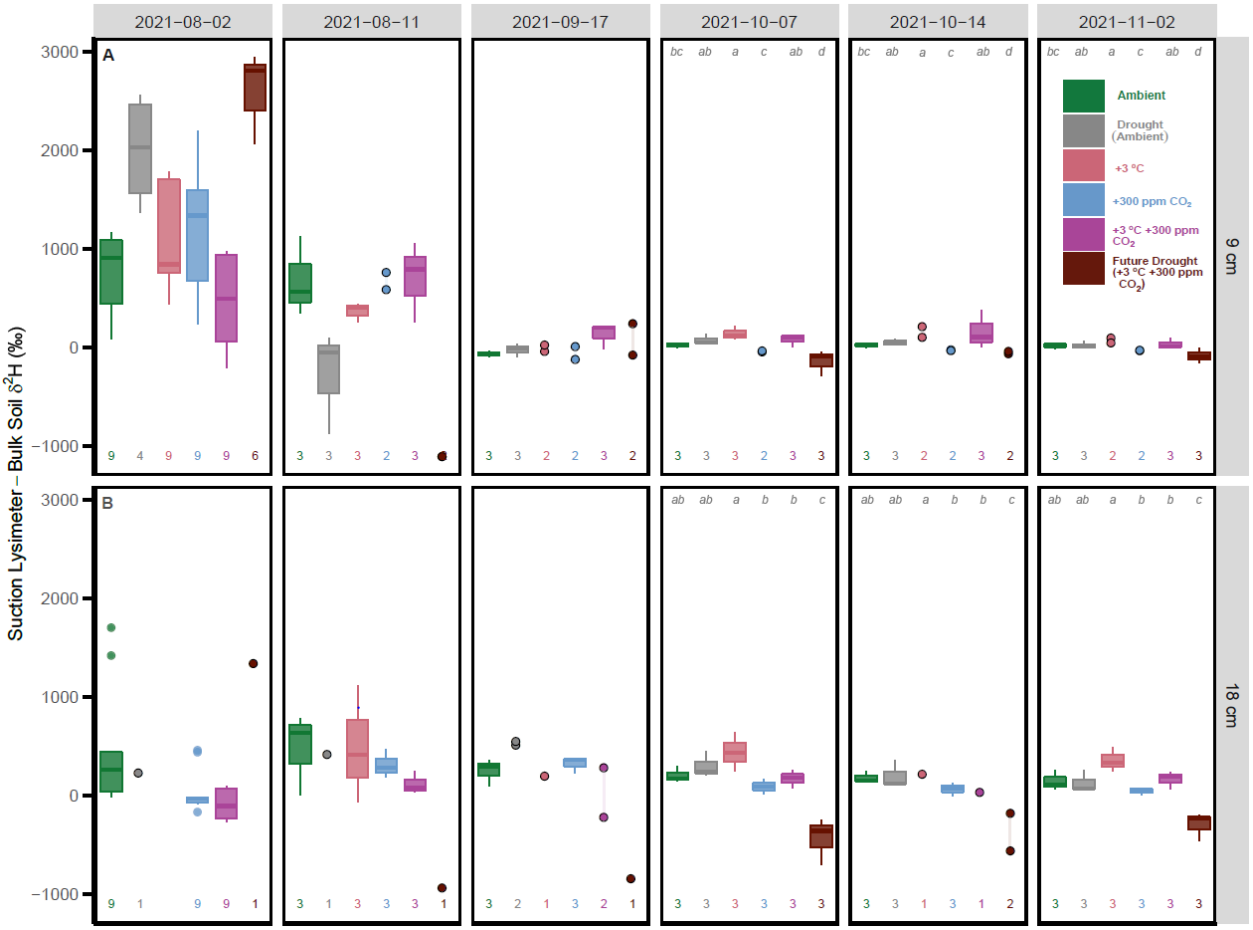


Fig. S9. **Mobile versus bulk soil water δ^2H**. Water stable isotope separation expressed as the difference between suction lysimeter and bulk soil water (from vapor membrane tubes) for the respective lysimeter sampling day at 9 (**A**) and 18 (**B**) cm depths. *Different letters* denote significant differences ($p < 0.05$) between treatments within each soil depth by combining data from the last three sampling times. Numbers on panel floors display *n* observations per treatment, depth, and sampling day (suction lysimeter $n > 3$ reflect x3, 2-h resolution sampling during label). Data are displayed as boxplots where $n \geq 3$, and as points for $n < 3$, which are connected by a line where $n = 2$.

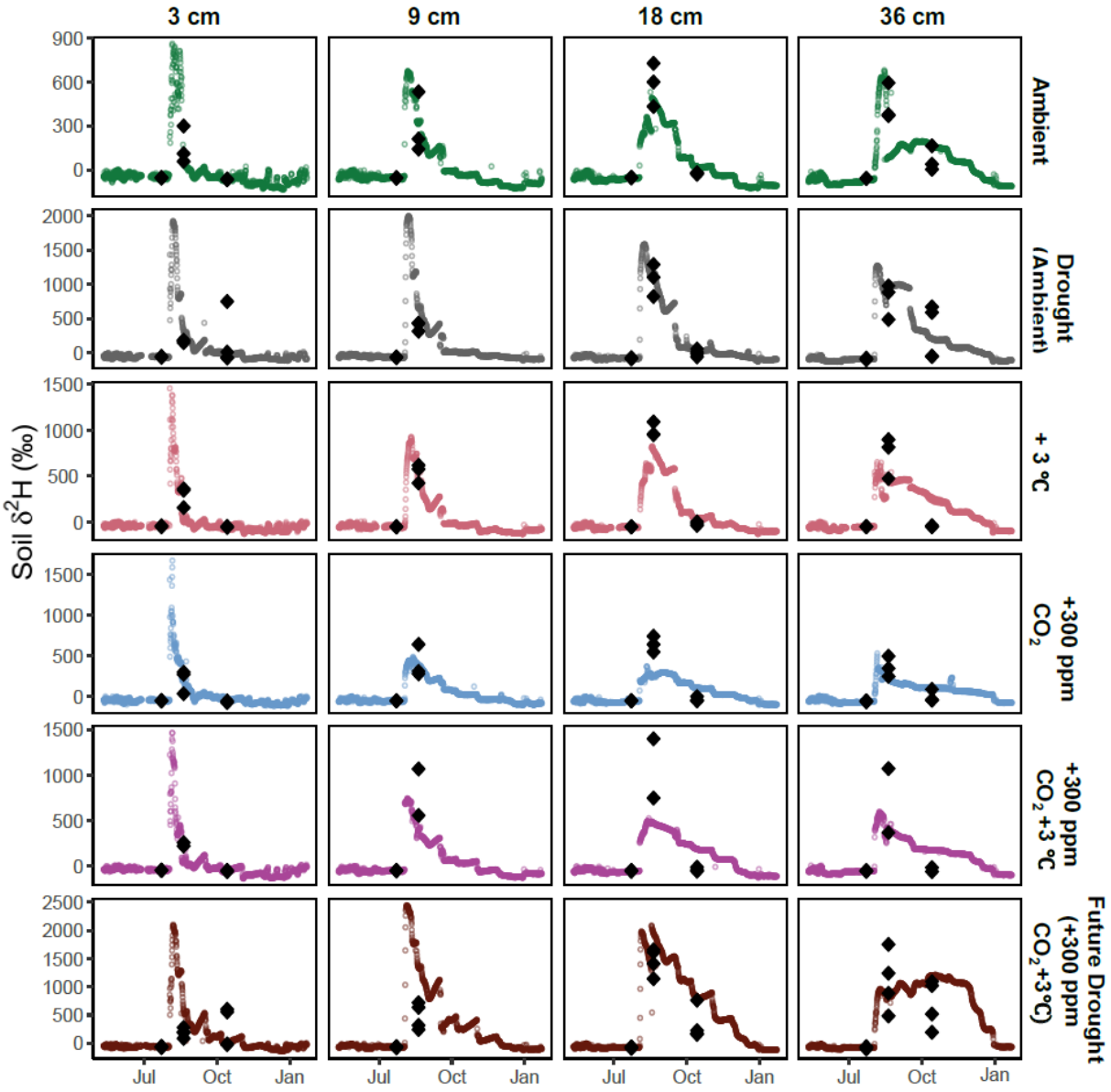


Fig. S10. High resolution δ^2H from membrane tube and destructive samples. ^2H signatures isotope values from membrane tubes across the six global change treatments between May 2021 and Jan 2022, with black diamonds denoting periodic, replicated, destructive samples via cryogenic extraction method *n* = 3-6 per treatment and sampling event).

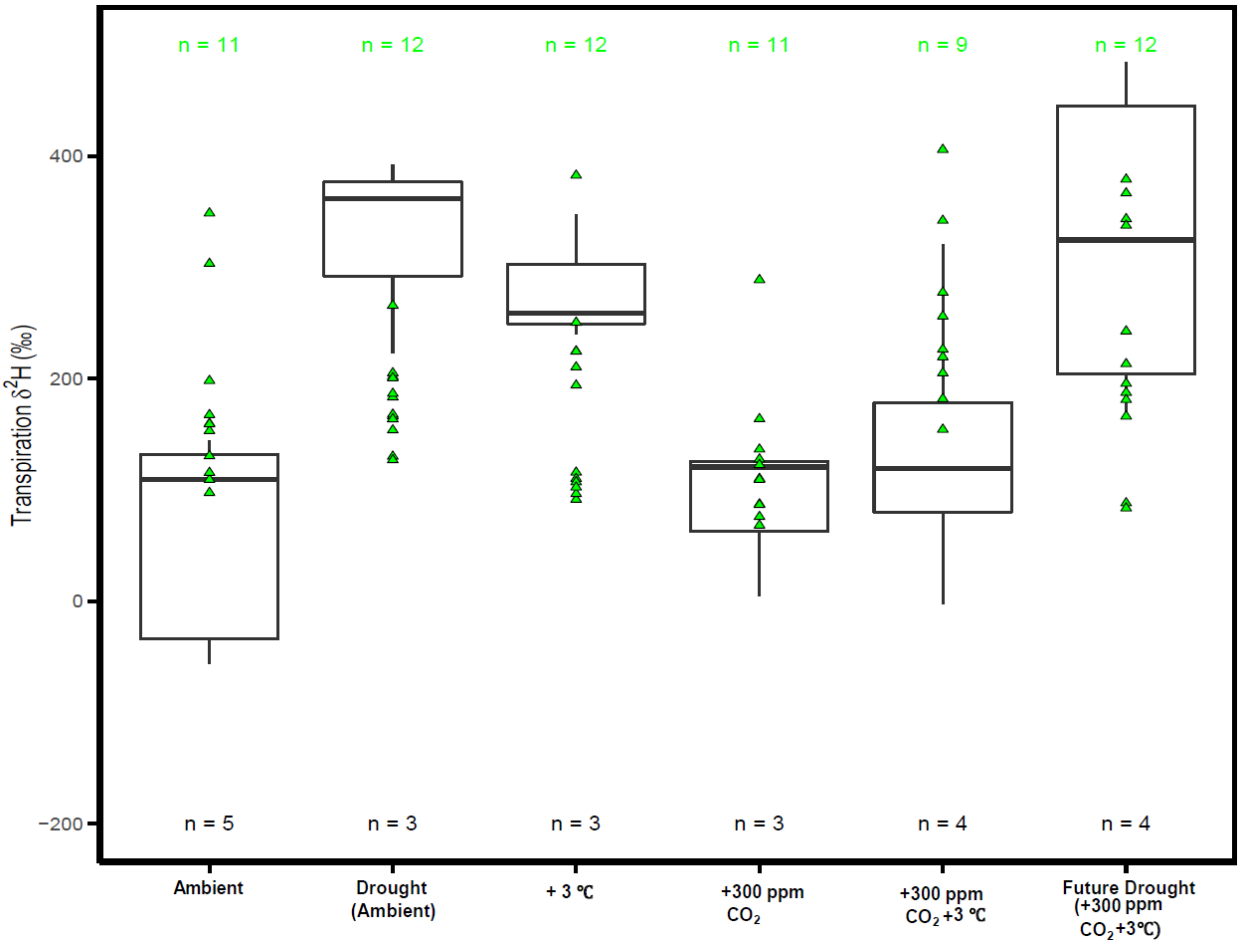


Fig. S11. **Leaf water and transpiration chamber transpiration estimates.** ^{2}H isotope values from transpiration chambers (boxplots; *n* per treatment and sampling event displayed in black) and destructive leaf samples (triangles; *n* per treatment and sampling event displayed in green) for the post-label period—20 days after the rewetting (2021-08-22)

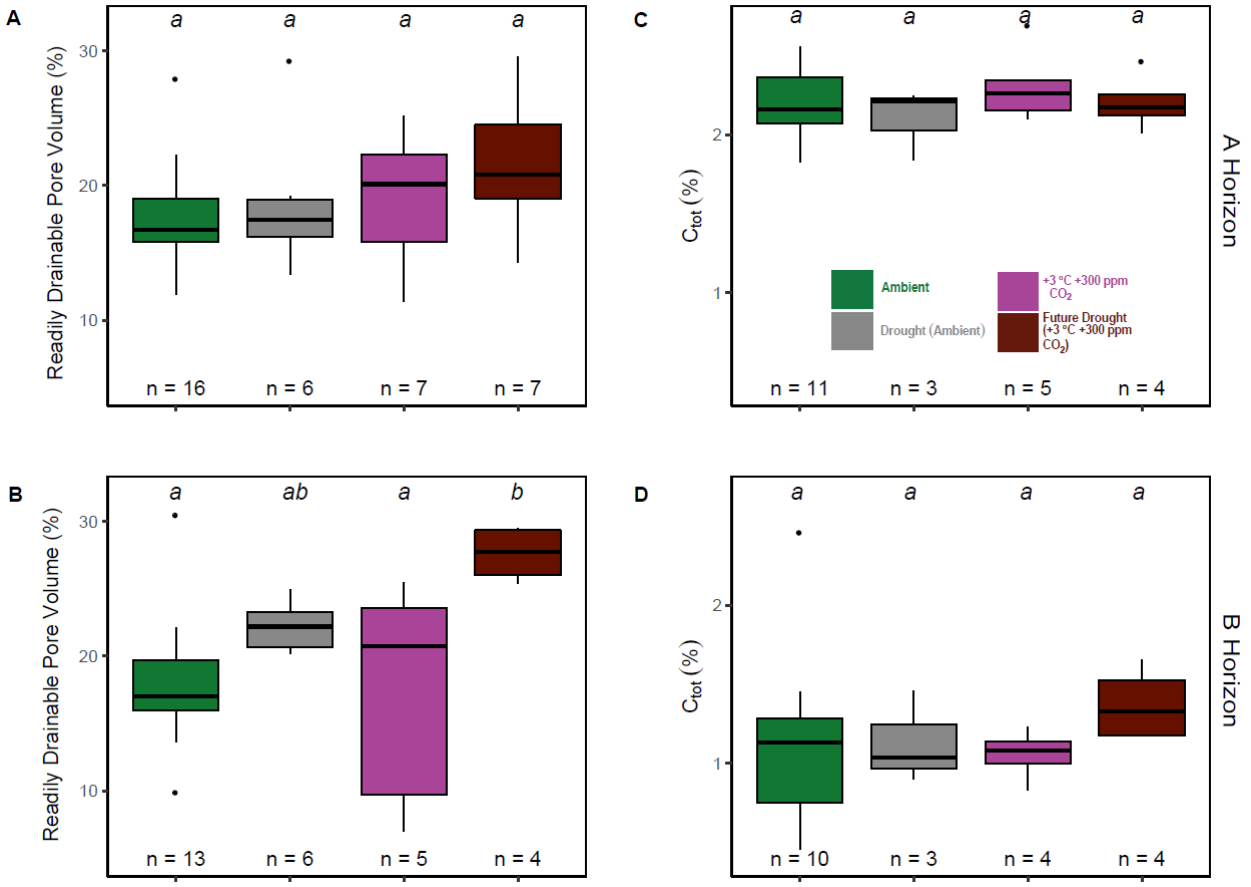


Fig. S12. Soil physiochemical properties. Soil readily drainable pore volume (**A** and **B**) and soil organic carbon content (**C** and **D**) for the four extreme treatments (*n* samples per treatment and depth plotted below boxplots) from soil cores taken from the A (5-10 cm; **B** and **D**) and B (35-40 cm; **A** and **C**) horizons. *Different letters* denote significant differences ($p < 0.05$) between treatments by soil horizon

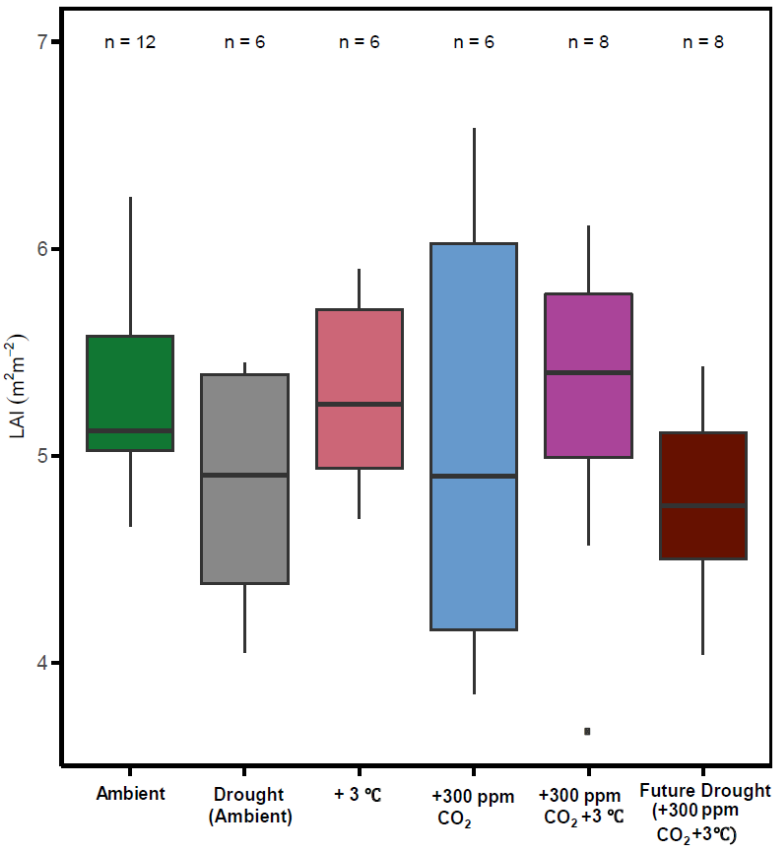


Fig. S13. End of 2021 growing season leaf area index (LAI). Measurements with an AccuPAr LP-80 from *n* = 3-6 replicate plots on 2024-09-14 and just before the final cut (2024-09-24). Pooled sample size is displayed above each boxplot.

.

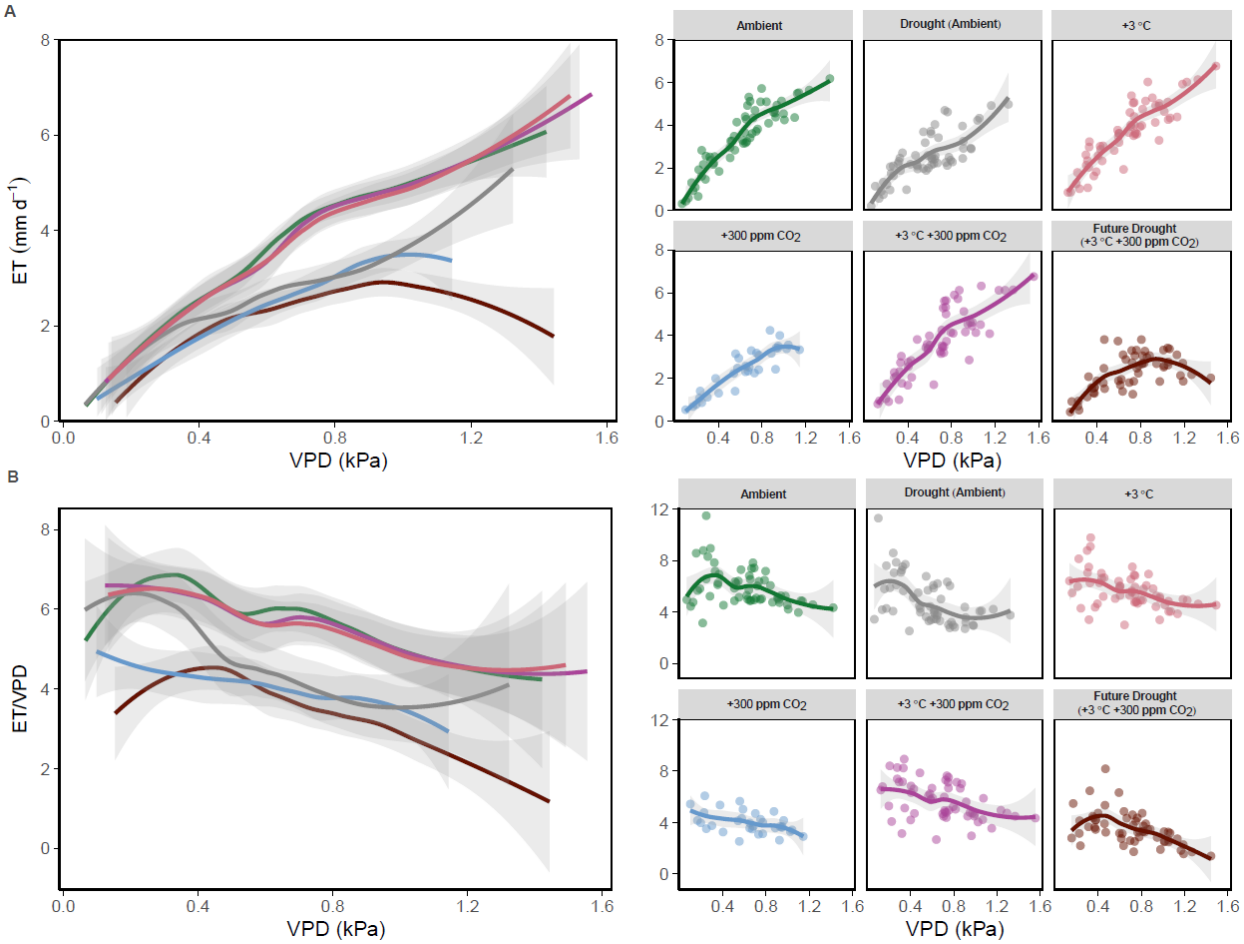


Fig. S14. Sensitivity of evapotranspiration and canopy conductance to vapor pressure deficit (VPD) during the period from the label application (2021-08-02) till the 3rd cut (2021-09-24). **A** shows the average daily eavpotranspiration (ET, mm d^{-1}) rate derived from weighable lysimeters (SFLs and LLs; *n* = 1-2 per treatment) versus daily (daytime) canopy vapor pressure defecit (VPD in kPa; *n* =1, per treatment) whereas **B** shows the same ET values normalilzed to VPD (ETVPD), defined here as canopy conductance. All relationships are plotted either together (left) or delineated by treatement (right). Grey bands denote 95% confidence intervals per treatment**.**

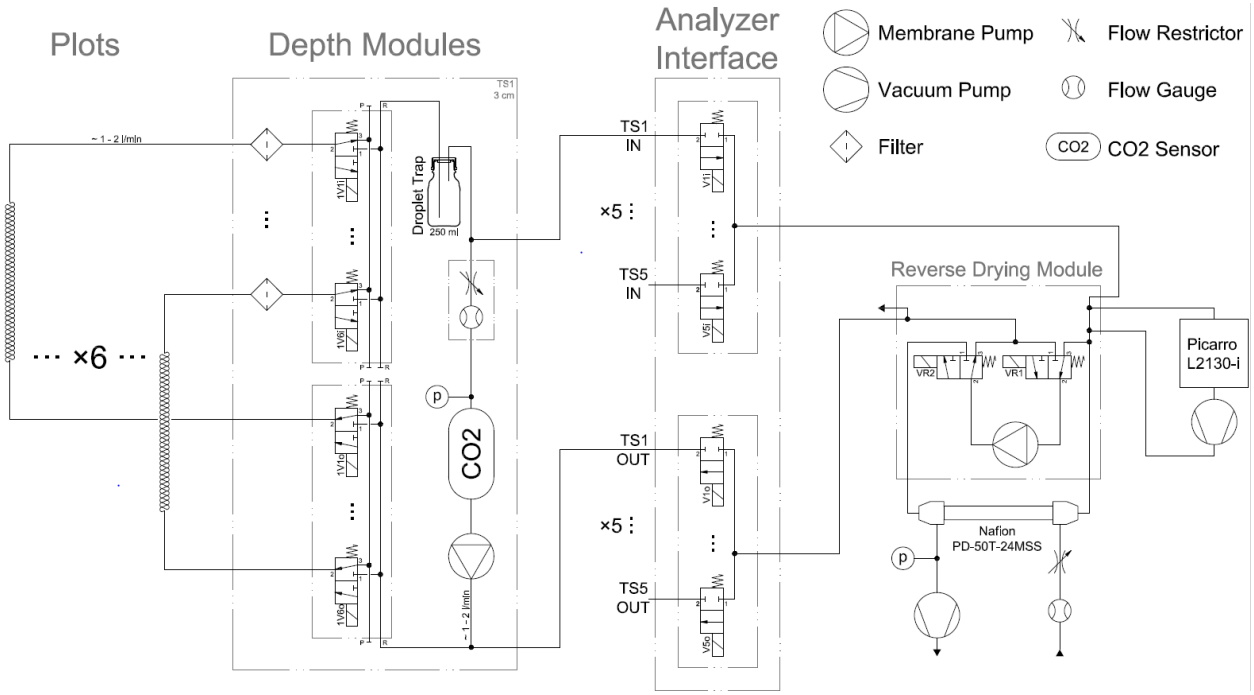


Fig. S15. **Schematic of membrane tube system**. Figure was made using AutoCAD 2019 software (AutoCAD, San Francisco California).

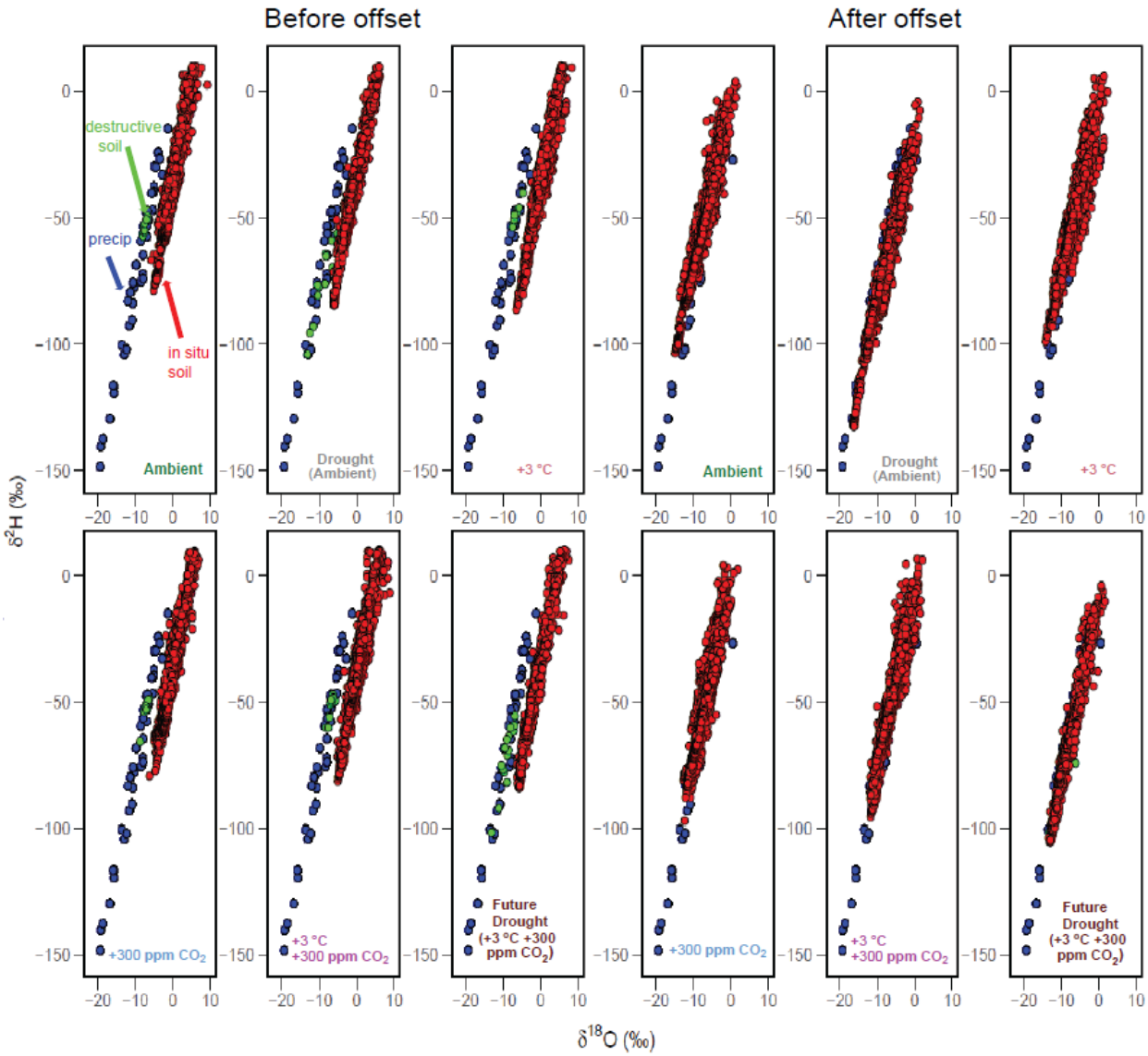


Fig. S16. **Membrane tube system isotopic offsets**. Example of membrane tube isotope data before and after offset using values taken under natural abundance conditions at peak drought

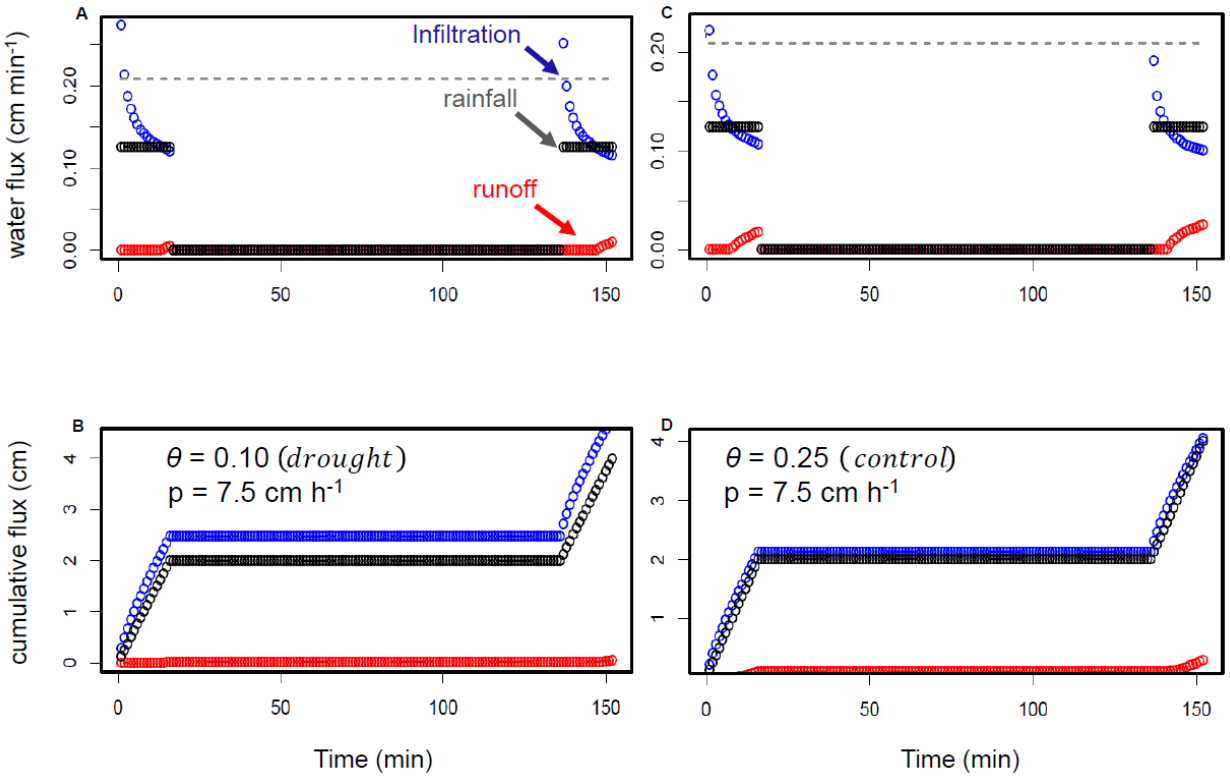


Fig. S17. **Infiltration modeling results for the rewetting rainfall simulation**. Exercise included an extremely dry soil (drought; **A** and **B**) and naturally moist (control; **C** and **D**) system at the time of the labeled rewetting. Dashed horizontal line represents the saturated hydraulic conductivity K_s.

Table S1. Summary of experimental drought for the years 2017-2021. θ_{min} is the minimum soil water content measured in the deep rootzone (36 cm) for the drought period. Note that an intense natural drought in 2018 prevented any experimental drought simulations for this year.

Ambient (Drought)				
	Precipitation Suppression (mm)	θ_{min}	Duration (d)	Dates
2017	382	0.17	65	2017-05-23 to 2017-07-27
2019	161	0.19	62	2019-04-18 to 2019-06-19
2020	201	0.19	40	2020-06-17 to 2020-07-27
2021	295	0.11	67	2021-05-27 to 2021-08-02

+300 ppm CO_2 & + 3 ℃ (Drought)				
	Precipitation Suppression (mm)	θ_{min}	Duration (d)	Dates
2017	382	0.14	65	2017-05-23 to 2017-07-27
2019	161	0.15	62	2019-04-18 to 2019-06-19
2020	201	0.14	40	2020-06-17 to 2020-07-27
2021	295	0.16	67	2021-05-27 to 2021-08-02

Table S2. General parameter descriptions for H1D simulations.

Parameter	Description
θ_r [%]	residual water content
θ_s [%]	saturated water content
α [-]	alpha Van Genuchten parameter
n [-]	n Van Genuchten parameter
K_s [cm day^{-1}]	saturated hydraulic conductivity
λ_L [cm^{-1}]	longitudinal dispersivity
τ [-]	tortuosity factor in the conductivity function

Table S3. Prior distribution for the model parameters for the inverse H1D calibration procedure. The prior distribution for saturated water content θ_s was different for the upper (0-30 cm) and lower layer (30-140 cm).

Parameter	Distribution	Range
θ_s 0-30 cm [%]	Normal	45±4
θ_s 30-140 cm [%]	Normal	40±4
α [cm^{-1}]	Uniform	0.001 – 0.15
n [-]	Uniform	1.05-1.7
K_s [cm day^{-1}]	Uniform	1-5000
λ_L [-]	Uniform	1-40

Table S4. Soil hydraulic properties and longitudinal dispersivity obtained from the best-fit inverse calibration with DREAM.

	Parameter	Ambient	+300 ppm CO_2	+ 3 ℃	+300 ppm CO_2 & + 3 ℃	Ambient (Drought)	+300 ppm CO_2 & + 3 ℃ (Drought)
0–30 cm	θ_s [%]	49.5	47.2	48.4	49.8	46.5	49.7
	α [-]	0.016	0.076	0.077	0.1558	0.147	0.151
	n [-]	1.21	1.14	1.20	1.17	1.21	1.17
	K_s [cm day^{-1}]	55	1395	773	2838	556	882
	λ_L [cm^{-1}]	23.4	27.1	29.2	33.7	17.0	6.6
30–140 cm	θ_s [%]	44.8	39.9	47.7	37.2	34.2	41
	α [-]	0.149	0.091	0.068	0.099	0.037	0.066
	n [-]	1.15	1.17	1.18	1.14	1.08	1.13
	K_s [cm day^{-1}]	3553	3313	3313	2312	3420	4935
	λ_L [cm^{-1}]	11.6	33.1	38.8	21.8	18.3	7.0
	λ_L [cm^{-1}]	11.6	33.1	38.8	21.8	18.3	7.0
0–140 cm	θ_r [%]	0.05	0.05	0.05	0.05	0.05	0.05
	τ [-]	0.5	0.5	0.5	0.5	0.5	0.5

Table S5. The inverse estimated parameters for this refined future drought H1D model.

	θ_s [%]	α [-]	n [-]	K_s [cm day^{-1}]	θ_{r-im} [%]	θ_{s-im} [%]	ω [-]	λ_L [cm^{-1}]
Layer 1	27.5	0.065	1.2	5000	1	20	0.2	15
Layer 2	27	0.065	1.2	1050	1	20	0.2	15

References

1. I. A. Shiklomanov, *Water in crisis. A guide to the world's fresh water resources*. (Oxford University Press 1993).
2. J. S. Caplan *et al.*, Decadal-scale shifts in soil hydraulic properties as induced by altered precipitation. *Science Advances* **5**, eaau6635 (2019).
3. P. D'Odorico, A. Porporato, Preferential states in soil moisture and climate dynamics. *Proceedings of the National Academy of Sciences* **101**, 8848-8851 (2004).
4. G. G. Amenu, P. Kumar, X.-Z. J. J. o. c. Liang, Interannual variability of deep-layer hydrologic memory and mechanisms of its influence on surface energy fluxes. *Journal of Climate* **18**, 5024-5045 (2005).
5. A. K. Knapp *et al.*, Rainfall variability, carbon cycling, and plant species diversity in a mesic grassland. *Science* **298**, 2202-2205 (2002).
6. L. Deng, K. Wang, J. Li, G. Zhao, Z. Shangguan, Effect of soil moisture and atmospheric humidity on both plant productivity and diversity of native grasslands across the Loess Plateau, China. *Ecological Engineering* **94**, 525-531 (2016).
7. J. K. Green *et al.*, Large influence of soil moisture on long-term terrestrial carbon uptake. *Nature* **565**, 476-479 (2019).
8. A. García-García *et al.*, Soil heat extremes can outpace air temperature extremes. *Nature Climate Change*, 1-5 (2023).
9. L. J. Bouaziz *et al.*, Ecosystem adaptation to climate change: the sensitivity of hydrological predictions to time-dynamic model parameters. *Hydrology and Earth System Sciences* **26**, 1295-1318 (2022).
10. K. A. Novick *et al.*, The increasing importance of atmospheric demand for ecosystem water and carbon fluxes. *Nature Climate Change* **6**, 1023-1027 (2016).
11. Z. Fu *et al.*, Atmospheric dryness reduces photosynthesis along a large range of soil water deficits. *Nature Communications* **13**, 1-10 (2022).
12. A. M. Ukkola *et al.*, Reduced streamflow in water-stressed climates consistent with CO2 effects on vegetation. *Nature Climate Change* **6**, 75-78 (2016).
13. H. Poorter *et al.*, A meta-analysis of responses of C3 plants to atmospheric CO2: dose–response curves for 85 traits ranging from the molecular to the whole-plant level. *New Phytologist* **233**, 1560-1596 (2022).
14. J. Roy *et al.*, Elevated CO2 maintains grassland net carbon uptake under a future heat and drought extreme. *Proceedings of the National Academy of Sciences* **113**, 6224-6229 (2016).
15. J. S. Mankin, R. Seager, J. E. Smerdon, B. I. Cook, A. P. J. N. G. Williams, Mid-latitude freshwater availability reduced by projected vegetation responses to climate change. *Nature Geoscience* **12**, 983-988 (2019).

16. A. L. Swann, F. M. Hoffman, C. D. Koven, J. T. Randerson, Plant responses to increasing CO2 reduce estimates of climate impacts on drought severity. *Proceedings of the National Academy of Sciences* **113**, 10019-10024 (2016).
17. J. A. Morgan *et al.*, C4 grasses prosper as carbon dioxide eliminates desiccation in warmed semi-arid grassland. *Nature* **476**, 202-205 (2011).
18. D. A. Robinson *et al.*, Global environmental changes impact soil hydraulic functions through biophysical feedbacks. *Global Change Biology* **25**, 1895-1904 (2019).
19. S. Zhou *et al.*, Soil moisture–atmosphere feedbacks mitigate declining water availability in drylands. *Nature Climate Change* **11**, 38-44 (2021).
20. M. A. Caretta, A. Mukherji, R. B. M. Arfanuzzaman, S. M. R. Morgan, M. Kumar, Water. In: Climate Change 2022: Impacts, Adaptation, and Vulnerability. Contribution of Working Group II to the Sixth Assessment Report of the Intergovernmental Panel on Climate Change. (2022).
21. G. Naumann *et al.*, Global changes in drought conditions under different levels of warming. *Geophysical Research Letters* **45**, 3285-3296 (2018).
22. K. Yue *et al.*, Influence of multiple global change drivers on terrestrial carbon storage: additive effects are common. *Ecology Letters* **20**, 663-672 (2017).
23. J. Song *et al.*, A meta-analysis of 1,119 manipulative experiments on terrestrial carbon-cycling responses to global change. *Nature Ecology & Evolution* **3**, 1309-1320 (2019).
24. Z. Xu, Y. Jiang, B. Jia, G. Zhou, Elevated-CO2 response of stomata and its dependence on environmental factors. *Frontiers in Plant Science* **7**, 657 (2016).
25. C. Werner *et al.*, Ecosystem fluxes during drought and recovery in an experimental forest. *Science* **374**, 1514-1518 (2021).
26. J. D. Hewlett, A. R. Hibbert, Factors affecting the response of small watersheds to precipitation in humid areas. *Forest Hydrology* **1**, 275-290 (1967).
27. J. H. Horton, R. H. Hawkins, Flow path of rain from the soil surface to the water table. *Soil Science* **100**, 377-383 (1965).
28. J. R. Brooks, H. R. Barnard, R. Coulombe, J. J. McDonnell, Ecohydrologic separation of water between trees and streams in a Mediterranean climate. *Nature Geoscience* **3**, 100 (2010).
29. J. Evaristo, S. Jasechko, J. J. McDonnell, Global separation of plant transpiration from groundwater and streamflow. *Nature* **525**, 91-94 (2015).
30. P. Hervé-Fernández *et al.*, Assessing the ‘two water worlds’ hypothesis and water sources for native and exotic evergreen species in south-central Chile. *Hydrological Processes* **30**, 4227-4241 (2016).
31. J. J. McDonnell, The two water worlds hypothesis: Ecohydrological separation of water between streams and trees? *Wiley Interdisciplinary Reviews: Water* **1**, 323-329 (2014).
32. J. Radolinski, L. Pangle, J. Klaus, R. D. Stewart, Testing the ‘two water worlds’ hypothesis under variable preferential flow conditions. *Hydrological Processes* **35**, e14252 (2021).
33. C. E. Finkenbiner, S. P. Good, J. Renée Brooks, S. T. Allen, S. J. N. C. Sasidharan, The extent to which soil hydraulics can explain ecohydrological separation. *Nature Communications* **13**, 6492 (2022).
34. J. Blair, J. Nippert, J. Briggs, *Ecology and the Environment, The Plant Sciences 8*. R. Monson, Ed., Grassland Ecology (Springer, 2014), vol. 389, pp. 389-423.

35. D. Reinthaler *et al.*, Responses of grassland soil CO2 production and fluxes to drought are shifted in a warmer climate under elevated CO2. *Soil Biology and Biochemistry* **163**, 108436 (2021).
36. *ClimGrassHydro - Ecohydrology of mountain grasslands under global change: mechanisms and consequences* (2023 https://epub.oeaw.ac.at/0xc1aa5576%200x003e4d29.pdf.
37. D. P. Van Vuuren *et al.*, The representative concentration pathways: an overview. *Climatic Change* **109**, 5-31 (2011).
38. J. Šimůnek, M. Šejna, H. Saito, M. Sakai, M. T. Van Genuchten, "The HYDRUS-1D software package for simulating the one-dimensional movement of water, heat, and multiple solutes in variably-saturated media," (University of California-Riverside Research Reports, 2018).
39. W. H. Bowers, J. J. Mercer, M. S. Pleasants, D. G. Williams, A combination of soil water extraction methods quantifies the isotopic mixing of waters held at separate tensions in soil. *Hydrology and Earth System Sciences* **24**, 4045-4060 (2020).
40. P. Deseano Diaz *et al.*, Insights into tension-mediated and antecedent water effects on soil water isotopic composition. *Vadose Zone Journal*, e20288 (2023).
41. P. Benettin *et al.*, Tracing and closing the water balance in a vegetated lysimeter. *Water Resources Research* **57**, e2020WR029049 (2021).
42. Y. Rothfuss, H. Vereecken, N. Brüggemann, Monitoring water stable isotopic composition in soils using gas-permeable tubing and infrared laser absorption spectroscopy. *Water Resources Research* **49**, 3747-3755 (2013).
43. J. Knighton, W. J. G. R. L. Berghuijs, Water Ages Explain Tradeoffs Between Long-Term Evapotranspiration and Ecosystem Drought Resilience. *Geophysical Research Letters* **50**, e2023GL103649 (2023).
44. J. S. Selker, J. T. McCord, C. K. Keller, *Vadose zone processes*. (CRC Press, 1999).
45. R. D. Stewart, D. E. Rupp, M. R. A. Najm, J. S. Selker, Modeling effect of initial soil moisture on sorptivity and infiltration. *Water Resources Research* **49**, 7037-7047 (2013).
46. J. Radolinski *et al.*, A spectrum of preferential flow alters solute mobility in soils. *Scientific Reports* **12**, 1-11 (2022).
47. N. Jarvis, A review of non-equilibrium water flow and solute transport in soil macropores: Principles, controlling factors and consequences for water quality. *European Journal of Soil Science* **58**, 523-546 (2007).
48. M. Sprenger *et al.*, The demographics of water: A review of water ages in the critical zone. *Reviews of Geophysics*, (2019).
49. W. Larcher, *Physiological plant ecology: ecophysiology and stress physiology of functional groups*. (Springer Science & Business Media, 2003).
50. N. B. Rodriguez, K. J. McGuire, J. Klaus, Time-Varying Storage–Water Age Relationships in a Catchment With a Mediterranean Climate. *Water Resources Research* **54**, 3988-4008 (2018).
51. J. Evaristo *et al.*, Characterizing the fluxes and age distribution of soil water, plant water, and deep percolation in a model tropical ecosystem. *Water Resources Research* **55**, 3307-3327 (2019).
52. L. Pires *et al.*, Micromorphological analysis to characterize structure modifications of soil samples submitted to wetting and drying cycles. *Catena* **72**, 297-304 (2008).

53. C. Terrer *et al.*, A trade-off between plant and soil carbon storage under elevated CO2. *Nature* **591**, 599-603 (2021).
54. B. Drigo *et al.*, Impacts of 3 years of elevated atmospheric CO 2 on rhizosphere carbon flow and microbial community dynamics. *Global Change Biology* **19**, 621-636 (2013).
55. L. Fuchslueger, M. Bahn, K. Fritz, R. Hasibeder, A. Richter, Experimental drought reduces the transfer of recently fixed plant carbon to soil microbes and alters the bacterial community composition in a mountain meadow. *New Phytologist* **201**, 916-927 (2014).
56. F. T. de Vries *et al.*, Soil bacterial networks are less stable under drought than fungal networks. *Nature Communications* **9**, 3033 (2018).
57. A. N. Koop *et al.*, Is macroporosity controlled by complexed clay and soil organic carbon? *Geoderma* **437**, 116565 (2023).
58. V. Forstner, M. Vremec, M. Herndl, S. Birk, Effects of dry spells on soil moisture and yield anomalies at a montane managed grassland site–a lysimeter climate experiment. *Ecohydrology*, e2518 (2023).
59. M. Vremec *et al.*, Sensitivity of evapotranspiration and seepage to elevated atmospheric CO2 from lysimeter experiments in a montane grassland. *Journal of Hydrology* **617**, 128875 (2023).
60. V. Forstner *et al.*, Response of water balance components to climate change in permanent grassland soil ecosystems. *Hydrology and Earth System Sciences*, 1-30 (2021).
61. C. Grossiord *et al.*, Plant responses to rising vapor pressure deficit. *New Phytologist* **226**, 1550-1566 (2020).
62. J. Denissen *et al.*, Widespread shift from ecosystem energy to water limitation with climate change. *Nature Climate Change* **12**, 677-684 (2022).
63. Y. Zhang *et al.*, Southern Hemisphere dominates recent decline in global water availability. *Science* **382**, 579-584 (2023).
64. A. Dai, Increasing drought under global warming in observations and models. *Nature Climate Change* **3**, 52-58 (2013).
65. M. Sprenger, S. T. Allen, Commentary: What ecohydrologic separation is and where we can go with it. *Water Resources Research*, e2020WR027238 (2020).
66. M. Sprenger, P. Llorens, C. Cayuela, F. Gallart, J. Latron, Mechanisms of consistently disjunct soil water pools over (pore) space and time. *Hydrology and Earth System Sciences* **23**, 2751-2762 (2019).
67. J. Radolinski *et al.*, Dataset for Radolinski et al. :"Drought in a warmer, CO2-rich climate restricts grassland water use and soil water mixing" [Dataset]. **Dryad**, (2024) http://datadryad.org/stash/share/si22ZWekx4W_0intZ5bny1A1bcSGQElQF4IYQbhJ7Ig.
68. H. P. Piepho, M. Herndl, E. Pötsch, M. Bahn, Designing an experiment with quantitative treatment factors to study the effects of climate change. *Journal of Agronomy and Crop Science* **203**, 584-592 (2017).
69. F. Miglietta *et al.*, Spatial and temporal performance of the MiniFACE (Free Air CO2 Enrichment) system on bog ecosystems in northern and central Europe. *Environmental Monitoring Assessment* **66**, 107-127 (2001).
70. B. A. Kimball *et al.*, Infrared heater arrays for warming ecosystem field plots. *Global Change Biology* **14**, 309-320 (2008).
71. M. Herndl, E. M. Pötsch, A. Bohner, M. Kandolf, Lysimeter als Bestandteil eines technischen Versuchskonzeptes zur Simulation der Erderwärmung im Grünland. **119-126**, (2011).

72. X. Luo *et al.*, Mapping the global distribution of C4 vegetation using observations and optimality theory. *Nature Communications* **15**, 1219 (2024).
73. C. A. Havrilla, J. B. Bradford, C. B. Yackulic, S. M. Munson, Divergent climate impacts on C3 versus C4 grasses imply widespread 21st century shifts in grassland functional composition. *Diversity and Distributions* **29**, 379-394 (2023).
74. K. Meeran *et al.*, Warming and elevated CO2 intensify drought and recovery responses of grassland carbon allocation to soil respiration. *Global Change Biology* **27**, 3230-3243 (2021).
75. A. Kübert *et al.*, Tracing plant source water dynamics during drought by continuous transpiration measurements: An in-situ stable isotope approach. *Plant, Cell & Environment* **46**, 133-149 (2022).
76. M. Dubbert *et al.*, Stable oxygen isotope and flux partitioning demonstrates understory of an oak savanna contributes up to half of ecosystem carbon and water exchange. *Frontiers in Plant Science* **5**, 530 (2014).
77. S. Newberry, D. Nelson, A. Kahmen, Cryogenic vacuum artifacts do not affect plant water-uptake studies using stable isotope analysis. *Ecohydrology*, (2017).
78. J. Fank, G. v. Unold, High-precision weighable field Lysimeter–a tool to measure water and solute balance parameters. *International Water Irrigation and Drainage* **27**, 28-32 (2007).
79. M. Vremec *et al.*, Sensitivity of montane grassland water fluxes to warming and elevated CO2 from local to catchment scale: A case study from the Austrian Alps. *Journal of Hydrology: Regional Studies* **56**, 101970 (2024).
80. A. Peters *et al.*, Towards an unbiased filter routine to determine precipitation and evapotranspiration from high precision lysimeter measurements. *Journal of Hydrology* **549**, 731-740 (2017).
81. H. Shen, B. A. Tolson, J. Mai, Time to update the split-sample approach in hydrological model calibration. *Water Resources Research* **58**, e2021WR031523 (2022).
82. C. Stumpp, W. Stichler, M. Kandolf, J. Šimůnek, Effects of land cover and fertilization method on water flow and solute transport in five lysimeters: A long-term study using stable water isotopes. *Vadose Zone Journal* **11**, (2012).
83. L. A. Richards, Capillary conduction of liquids through porous mediums. *Physics* **1**, 318-333 (1931).
84. M. T. Van Genuchten, A closed-form equation for predicting the hydraulic conductivity of unsaturated soils 1. *Soil Science Society of America journal* **44**, 892-898 (1980).
85. J. T. Ritchie, Model for predicting evaporation from a row crop with incomplete cover. *Water Resources Research* **8**, 1204-1213 (1972).
86. R. A. Feddes, in *Simulation of plant growth and crop production*. (Pudoc, 1982), pp. 194-209.
87. G. J. Hoffman, M. T. Van Genuchten, *Soil properties and efficient water use: water management for salinity control*. Limitations to Efficient Water Use in Crop Production (ASA-CSSA-SSSA, Madison, WI, USA, 1983), pp. 73-85.
88. N. Jarvis, *The MACRO Model (version 3.1). Technical description and sample simulations*. (1994).
89. J. Bear, *Dynamics of fluids in porous media*. (Courier Corporation, 2013).

90. J. A. Vrugt, Markov chain Monte Carlo simulation using the DREAM software package: Theory, concepts, and MATLAB implementation. *Environmental Modelling* **75**, 273-316 (2016).
91. Y. Liu, J. Fernández-Ortega, M. Mudarra, A. Hartmann, Pitfalls and a feasible solution for using KGE as an informal likelihood function in MCMC methods: DREAM (ZS) as an example. *Hydrology and Earth System Sciences* **26**, 5341-5355 (2022).
92. A. Kübert *et al.*, Water Stable Isotopes in Ecohydrological Field Research: Comparison between In Situ and Destructive Monitoring Methods to Determine Soil Water Isotopic Signatures. *Frontiers in Plant Science* **11**, 387 (2020).
93. K. Kühnhammer *et al.*, Investigating the root plasticity response of Centaurea jacea to soil water availability changes from isotopic analysis. *New Phytologist* **226**, 98-110 (2020).
94. E. J. Oerter, A. Perelet, E. Pardyjak, G. Bowen, Membrane inlet laser spectroscopy to measure H and O stable isotope compositions of soil and sediment pore water with high sample throughput. *Rapid Communications in Mass Spectrometry* **31**, 75-84 (2017).
95. M. Beyer, K. Kühnhammer, M. J. H. Dubbert, E. S. Sciences, In situ measurements of soil and plant water isotopes: a review of approaches, practical considerations and a vision for the future. *Hydrology and Earth System Sciences* **24**, 4413-4440 (2020).
96. J. Horita, D. Wesolowski, Liquid-vapor fractionation of oxygen and hydrogen isotopes of water from the freezing to the critical temperature. *Geochimica et Cosmochimica Acta* **58**, 3425-3437 (1994).
97. R. van Geldern, J. A. C. Barth, Optimization of instrument setup and post-run corrections for oxygen and hydrogen stable isotope measurements of water by isotope ratio infrared spectroscopy (IRIS). *Limnology & Oceanography* **10**, 1024-1036 (2012).
98. C. Walker, J.-P. J. o. H. Brunel, Examining evapotranspiration in a semi-arid region using stable isotopes of hydrogen and oxygen. *Journal of Hydrology* **118**, 55-75 (1990).
99. L. Wang, S. P. Good, K. K. Caylor, L. A. Cernusak, Direct quantification of leaf transpiration isotopic composition. *Agricultural and Forest Meteorology* **154**, 127-135 (2012).
100. M. Schmidt *et al.*, Concentration effects on laser-based δ18O and δ2H measurements and implications for the calibration of vapour measurements with liquid standards. *Rapid Communications in Mass Spectrometry* **24**, 3553-3561 (2010).
101. S. P. Good *et al.*, δ2H isotopic flux partitioning of evapotranspiration over a grass field following a water pulse and subsequent dry down. *Water Resources Research* **50**, 1410-1432 (2014).
102. K. Soderberg, S. P. Good, L. Wang, K. J. V. Z. J. Caylor, Stable isotopes of water vapor in the vadose zone: A review of measurement and modeling techniques. *Vadose Zone Journal* **11**, vzj2011.0165 (2012).
103. H. Craig, L. I. Gordon, Deuterium and oxygen 18 variations in the ocean and the marine atmosphere. *Stable Isotopes in Oceanographic Studes and Paleotemperatures*, (1965).
104. J. Horita, D. Wesolowski, Liquid-vapor fractionation of oxygen and hydrogen isotopes of water from the freezing to the critical temperature. **58**, 3425-3437 (1994).
105. A. L. Buck, New equations for computing vapor pressure and enhancement factor. *Journal of Applied Meteorology Climatology* **20**, 1527-1532 (1981).
106. O. Tetens, Uber einige meteorologische Begriffe. *Z. Geophys* **6**, 297-309 (1930).

107. L. Merlivat, Molecular diffusivities of H 2 16 O, HD 16 O, and H 2 18 O in gases. *Journal of Chemical Physics* **69**, 2864-2871 (1978).
108. X. Sun *et al.*, Isotopic partitioning of evapotranspiration in a mesic grassland during two wetting–drying episodes. *Agricultural and Forest Meteorology* **301**, 108321 (2021).
109. R. Mathieu, T. Bariac, An isotopic study (2H and 18O) of water movements in clayey soils under a semiarid climate. *Water Resources Research* **32**, 779-789 (1996).
110. J. R. J. S. s. Philip, The theory of infiltration: 4. Sorptivity and algebraic infiltration equations. *Soil Science* **84**, 257-264 (1957).
111. J. Philip, Inverse solution for one-dimensional infiltration, and the ratio A/K1. *Water Resources Research* **26**, 2023-2027 (1990).
112. W. A. Dorigo *et al.*, Global automated quality control of in situ soil moisture data from the International Soil Moisture Network. *Vadose Zone Journal* **12**, (2013).
113. E. Z. Bean, R. G. Huffaker, K. W. J. V. Z. J. Migliaccio, Estimating field capacity from volumetric soil water content time series using automated processing algorithms. *Vadose Zone Journal* **17**, 1-12 (2018).
114. K. Beven, P. Germann, Macropores and water flow in soils revisited. *Water Resources Research* **49**, 3071-3092 (2013).
115. A. Mdaghri Alaoui, P. Germann, L. Lichner, V. Novak, Preferential transport of water and 131 Iodide in a clay loam assessed with TDR-techniques and boundary-layer flow theory. *Hydrology and Earth System Sciences* **1**, 813-822 (1997).
116. D. R. Nielsen, J. W. Biggar, K. T. Erh, Spatial variability of field-measured soil-water properties. *Hilgardia*, (1973).
117. A. Bargués-Tobella, L. A. Winowiecki, D. Sheil, T. G. Vågen, Determinants of Soil Field-Saturated Hydraulic Conductivity Across Sub-Saharan Africa: Texture and Beyond. *Water Resources Research* **60**, e2023WR035510 (2024).
118. N. K. Twarakavi, M. Sakai, J. J. W. R. R. Šimůnek, An objective analysis of the dynamic nature of field capacity. *Water Resources Research* **45**, (2009).
119. L. Richards, L. Weaver, Moisture retention by some irrigated soils as related to soil moisture tension. *Journal of Agricultural Research* **69**, 215 (1944).
120. W. Rawls, D. Gimenez, R. Grossman, Use of soil texture, bulk density, and slope of the water retention curve to predict saturated hydraulic conductivity. *Transactions of the ASAE* **41**, 983 (1998).
121. D. R. Hirmas *et al.*, Climate-induced changes in continental-scale soil macroporosity may intensify water cycle. *Nature* **561**, 100 (2018).
122. V. Filipović, Y. Coquet, H. H. Gerke, Representation of Plot-Scale Soil Heterogeneity in Dual-Domain Effective Flow and Transport Models with Mass Exchange. *Vadose Zone Journal* **18**, 1-14 (2019).
123. H. J. Vogel *et al.*, A holistic perspective on soil architecture is needed as a key to soil functions. *European Journal of Soil Science* **73**, e13152 (2022).
124. M. Tissink *et al.*, Individual Versus Combined Effects of Warming, Elevated CO2 and Drought on Grassland Water Uptake and Fine Root Traits. *Plant, Cell & Environment*, (2024).